Thermoacoustic boundary layers near the liquid-vapor critical point

K. A. Gillis, I. I. Shinder, and M. R. Moldover
Process Measurements Division, National Institute of Standards and Technology, Gaithersburg, Maryland 20899-8360, USA
(Received 8 January 2004; published 4 August 2004)

We measure and calculate the sound attenuation within thermoacoustic boundary layers between solid surfaces and xenon at its critical density ρ_c as the reduced temperature $\tau \equiv (T-T_c)/T_c$ approaches zero. (T_c is the critical temperature.) Using the known thermophysical properties of xenon, we predict that the attenuation at the boundary first increases approximately as $\tau^{-0.6}$ and then saturates when the effusivity of the xenon exceeds that of the solid. [The effusivity is $\varepsilon \equiv (\rho C_P \lambda_T)^{1/2}$, where C_P is the isobaric specific heat and λ_T is the thermal conductivity.] The model correctly predicts (±1.0%) the quality factors Q of resonances measured in a stainless steel resonator (ε_{ss}=6400 kg K^{-1} s$^{-5/2}$); it also predicts the observed increase of the Q, by up to a factor of 8, when the resonator is coated with a polymer (ε_{pr}=370 kg K^{-1} s$^{-5/2}$). The test data span the frequency range $0.1 < f < 7.5$ kHz and the reduced temperature range $10^{-3} < \tau < 10^{-1}$. We also predict that the thickness δ_T of the thermal boundary layer in the xenon decreases approximately as $\tau^{0.4}$ until $2\pi f \gamma \zeta/(\rho c^2) \approx 0.5$. ($\zeta$ is the bulk viscosity, γ is the heat capacity ratio, and c is the speed of sound.) Still closer to T_c, δ_T becomes complex and its magnitude increases. These predictions concerning δ_T have not yet been tested. We deduce accurate values for the heat capacity C_V and thermal conductivity λ_T for xenon in the range $10^{-3} < \tau < 10^{-1}$.

DOI: 10.1103/PhysRevE.70.021201 PACS number(s): 51.40.+p, 51.20.+d, 43.20.+g, 64.60.Fr

I. INTRODUCTION

We plan to determine the bulk viscosity of xenon ten times closer [in reduced temperature $\tau \equiv (T-T_c)/T_c$] to its liquid-vapor critical point than has been possible heretofore [1], to our knowledge. To do so, we must measure the dispersion and attenuation of sound at frequencies 1/100 of those used previously. As a first step, we measured the frequency response of a compact, acoustic resonator filled with xenon at its critical density ρ_c. From the frequency-response data in the range $100 < f < 7500$ Hz, we obtained the resonance frequency and the attenuation for six resonant modes. In general, the attenuation has contributions from the bulk viscosity acting throughout the volume of the xenon as well as contributions from the shear viscosity and the thermal conductivity acting within thin thermoacoustic boundary layers at the interface between the xenon and the solid walls of the resonator. Thus we can determine the bulk viscosity only when the boundary layer attenuation is small and well understood. In this paper, we show that the attenuation from the boundary layers in our stainless steel resonator is indeed understood to within 1%. (Unless otherwise noted, standard uncertainty is used throughout this paper.) Furthermore, we show that the boundary attenuation is decreased by as much as a factor of 8 by coating the interior surfaces of the resonator with a thin layer of a polymer that conducts heat poorly.

The present data span the reduced temperature range $10^{-3} < \tau < 10^{-1}$. These data test our understanding of thermoacoustic boundary layers because τ is small enough that the singularities in the thermophysical properties of xenon play a prominent role in the boundary attenuation. However, τ is large enough that the bulk viscosity makes only a small contribution to the attenuation. In the future, we will analyze the results closer to T_c, where we expect the bulk viscosity to dominate the attenuation and where gravitational stratification plays an important role.

A standard model of the thermoacoustic boundary layer [e.g., Eq. (9) in Ref. [2]] combined with the known thermophysical properties of near-critical xenon predicts that the boundary attenuation is proportional to $\tau^{-0.6}$ for $\tau > 10^{-3}$ and then crosses over to $\tau^{-0.8}$ in the fully asymptotic region close to T_c. The present data disagreed with this prediction and led us to refine the model of thermoacoustic boundary layers for near critical fluids. The refined model predicts three phenomena that do not appear in the standard model. First, the boundary attenuation increases as $\tau^{-0.6}$ (0.6 is an effective exponent) as $\tau \to 0$ for $\tau > 10^{-3}$ as before; however, the increase saturates when the effusivity of the xenon exceeds that of the solid wall. [The effusivity is $\varepsilon \equiv (\rho C_P \lambda_T)^{1/2}$, where C_P is the isobaric specific heat and λ_T is the thermal conductivity.] Second, the thickness δ_T of the thermal boundary layer depends upon the bulk viscosity ζ, and δ_T decreases as $\tau^{0.4}$ (0.4 is the observed effective exponent) as $\tau \to 0$ until a minimum is reached at the condition

$$\frac{\gamma \omega \zeta}{\rho c^2} \approx 0.5. \tag{1}$$

(Here, $\gamma \equiv C_P/C_V$ and $\omega \equiv 2\pi f$.) Third, still closer to T_c, δ_T becomes complex and its magnitude increases. When δ_T becomes complex, the spatial dependence of the thermal wave changes; also, the usual phase relationship between the temperature and pressure changes. These predictions concerning δ_T have not been tested to date.

Previously, Carlés and Zappoli [3] discussed the thermal relaxation of a near-critical fluid confined between two semi-infinite, insulating walls. They applied a heat flux at one wall and calculated the evolution of the temperature, pressure, and fluid velocity. (In contrast with this work, heat transfer

did not occur within either wall.) They found that the character of the temperature relaxation depended on whether the initial temperature of the fluid T_{initial} was above or below the characteristic temperature $T_{\text{Transition}}$. As T_{initial} approached $T_{\text{Transition}}$ from above, temperature gradients in their model relaxed via the piston effect at increasing rates while the time-dependent pressure remained nearly homogeneous throughout the fluid. When T_{initial} was less than $T_{\text{Transition}}$, temperature gradients relaxed more slowly as T_c was approached. This slowing down occurs when the bulk viscosity becomes large enough that pressure gradients develop near the walls impeding the thermal expansion (piston effect). The authors referred to the regions of T_{initial} above and below $T_{\text{Transition}}$ as "classical" and "viscous" regimes, respectively. At $T_{\text{Transition}}$, the viscous stress first reaches the same order of magnitude as the time-dependent pressure.

We identify $T_{\text{transition}}$ defined by Carlés and Zappoli with the temperature at which Eq. (1) holds. Our calculation includes heat flow in the walls; we find that the magnitude of the viscous stress is limited by the effusivity of the walls. For the polymer walls that we used, the viscous stresses were significantly less than the acoustic pressure. In a future publication, we shall present a more complete discussion of the influence of the bulk viscosity on acoustic measurements.

The results reported here were obtained with a double-Helmholtz acoustic resonator consisting of two cylindrical chambers connected by a small circular tube (see Fig. 1). In its lowest-frequency mode, the enclosed xenon oscillated between the chambers through the connecting tube. This mode is particularly advantageous for studies of near-critical fluids because it has a low frequency corresponding to an acoustic wavelength of 51 cm, yet the resonator is only 4.8 cm long and 2.35 cm high. Thus this resonator is easily thermostatted and stratification of the near-critical xenon in the Earth's gravitational field is insignificant in the data reported here. Resonators of this type are also useful for measurements of shear viscosity in dilute gases and, for such applications, are referred to as Greenspan viscometers. Recent publications [2,4–6] describe the theory of the Greenspan viscometer and its application to shear viscosity measurements in eight gases. When our resonator was filled with a dilute gas and driven with an acoustic transducer, the primary damping occurred in the viscous and thermal boundary layers characterized by the gas's viscous diffusivity $D_v \equiv \eta/\rho$ (also called the kinematic viscosity) and thermal diffusivity $D_T \equiv \lambda_T/(\rho C_P)$, respectively. In dilute gases, these *surface* damping mechanisms are orders of magnitude larger than the viscous and thermal *volume* processes that contribute to the so-called "classical" attenuation of freely propagating waves. A third damping process occurs throughout the volume of polyatomic fluids and fluids near their critical points. The associated transport property is the bulk viscosity ζ, and it causes significant attenuation when the product of the acoustic frequency and the relaxation time is order unity [7,8].

Kirchhoff [9] was the first to develop a theory for acoustic attenuation in dilute gases due to heat flow near a rigid wall with infinite heat capacity and infinite thermal conductivity. We refer to such a wall as a *perfect wall*. Dissipation near a wall occurs because the boundary conditions imposed on the fluid produce large velocity and temperature gradients there.

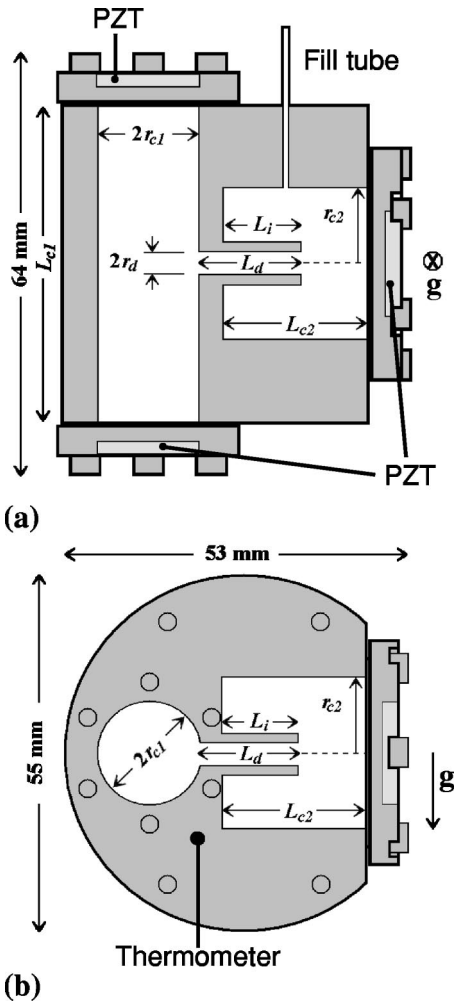

FIG. 1. Cross sectional views of the resonator are shown from (a) the top and (b) the side, relative to the direction of gravity (g). The nominal dimensions (in mm) were: $2r_{c1}=16$, $L_{c1}=48$, $2r_{c2}=23.5$, $L_{c2}=22$, $2r_d=4$, $L_d=15$, and $L_i=10.5$.

Far from the wall, the temperature oscillates with amplitude[1] $\tilde{T}_0 \approx (\gamma-1)T\,\tilde{p}_0/(\rho c^2)$ due to the nearly adiabatic pressure oscillations with amplitude $\tilde{p}_0$. (T is the average temperature.) The temperature amplitude decreases exponentially from $\tilde{T}_0$ to zero at the perfect wall with the characteristic thermal penetration length $\delta_T \approx (2D_T/\omega)^{1/2}$. [Equation (A19) is the exact expression for δ_T.] The length δ_T is the distance that heat can diffuse during one acoustic cycle; in this work $0.5 < \delta_T < 10$ μm. The oscillating temperature gradient is on the order $\tilde{T}_0/\delta_T$; it drives heat flow between the fluid and the wall, and it shifts the phase between the pressure and density oscillations. Because of this phase shift, the acoustic wave does irreversible work. The rate of acoustic energy loss per unit area due to heat flow near a wall is of order $\lambda_T \tilde{T}_0^2/(T\delta_T)$.

Viscous friction imposes a no-slip boundary condition on the acoustic velocity $\tilde{\mathbf{u}}$ at the wall. That is, the tangential component of $\tilde{\mathbf{u}}$ is zero at the resonator's wall. Far from the wall, $\tilde{\mathbf{u}}$ oscillates with amplitude $\tilde{u}_0 \approx \tilde{p}_0/(\rho c)$. The velocity

[1]We use a tilde to distinguish acoustic fields from average values.

oscillations exponentially vanish over the distance $\delta_v = (2D_v/\omega)^{1/2} \approx 10$ μm, where D_v is called either the viscous diffusivity or the kinematic viscosity. The velocity gradient near the wall is of order $\tilde{u}_0/\delta_v$; therefore the rate of acoustic energy loss per unit area due to viscous friction is of order $\eta\tilde{u}_0^2/\delta_v$.

To lowest order in the quantities (δ_v/L) and (δ_T/L), where L is the smallest physical dimension of the resonator, the fractional energy lost per cycle for a given mode of a *dilute* gas enclosed by a perfect wall is [2,10]

$$Q^{-1} = q_v\delta_v + (\gamma - 1)q_T\delta_T + \frac{\omega\zeta}{\rho c^2}, \tag{2}$$

where Q is the quality factor for the mode, and q_v and q_T are mode-dependent geometric factors. A more general form of Eq. (2) is discussed in Sec. II. For geometries with a high degree of symmetry, q_v and q_T can be calculated analytically from perturbation theory. For more complicated geometries, q_v and q_T can be determined from numerical calculation or from calibration measurements with a well-characterized gas far from its critical point. The term $\omega\zeta/(\rho c^2)$ in Eq. (2) is negligible in dilute gases, except for polyatomic gases that have internal modes which relax on a time scale comparable to the acoustic period or in gases so dilute that the mean free path becomes a significant fraction of the wavelength of sound.

As the fluid approaches its liquid-vapor critical point, the effusivity of the fluid increases as $\tau^{-0.8}$. When the effusivity of the fluid approaches the effusivity of the solid, Kirchhoff's "perfect wall" approximation fails. Then heat exchange between the fluid and the solid modulates the temperature of the boundary and a temperature wave penetrates the solid. At smaller values of τ, most of the temperature gradient occurs in the solid. Then, the generation of entropy and the thermal boundary dissipation near the critical point are determined by the effusivity of the solid, a quantity that is independent of τ.

For values of τ equal to or smaller than those spanned by the present data, the damping from bulk viscosity and thermal diffusivity is much larger than damping from the viscous diffusivity. The very weak divergence of the shear viscosity $(\tau^{-0.043})$ is barely detectable in the present experiments.

II. ACOUSTIC MODEL

Morse and Ingard [8] present a theory of acoustic attenuation in free space and near a solid boundary. However, their theory neglects the thermal wave in the solid, and it assumes that the attenuation is a small perturbation. Others [10,11] have published extensions of the theory that include the thermal and mechanical properties of the solid boundary, but these extensions also assume that D_v, D_T, and $\gamma - 1$ are small. We extend the theory to include the thermal wave in a rigid boundary, but we do not assume the attenuation is small. The present theory is valid close to the liquid-vapor critical point (one-phase region), where the dissipation is large and the heat transport in the solid is significant.

The governing equations for the thermal boundary layer dissipation are functions of the time-dependent fields $\tilde{p}$, $\tilde{\rho}$, $\tilde{T}$, $\tilde{s}$, and $\tilde{\mathbf{u}}$. These fields represent the fluctuating pressure, density, temperature, entropy per unit mass, and fluid (acoustic) velocity, respectively, and have time dependence $e^{i\omega t}$ by convention. Throughout this discussion, we assume the amplitudes of the fluctuating fields $\tilde{p}$, $\tilde{\rho}$, $\tilde{T}$, and $\tilde{s}$ are small compared to their average values P, ρ T, and S. The amplitude of $\tilde{\mathbf{u}}$ is assumed to be small compared to the speed of sound c. Near the critical point, we further restrict the magnitudes of the fluctuating fields to be small compared to the average distance from the critical point, i.e., $\tilde{T} \ll (T - T_c)$, $\tilde{p} \ll (P - P_c)$, and $\tilde{\rho} \ll (\rho - \rho_c)$, to ensure that the sound wave does not influence the critical behavior. Local thermodynamic equilibrium is tacitly assumed. Thus hydrodynamics with no-slip, no-temperature-jump boundary conditions is appropriate. To ensure local equilibrium, we require that the wavelength, the thicknesses of the boundary layers, and the dimensions of the resonator be larger than the correlation length or the mean free path, whichever is larger. The smallest boundary layer thickness for this work was $\sim 2\times 10^{-7}$ m at $\tau \approx 1\times 10^{-3}$. At this temperature, the correlation length was $\sim 1\times 10^{-8}$ m, and the mean free path was $\sim 3\times 10^{-10}$ m. Local equilibrium is therefore assured for the present work. Furthermore, we estimate that the boundary layer thickness (at audio frequencies) will be larger than the correlation length as close as $\tau \approx 1\times 10^{-5}$.

With these definitions, the basic equations are the linearized Navier-Stokes equation

$$\rho\frac{\partial\tilde{\mathbf{u}}}{\partial t} = -\boldsymbol{\nabla}\tilde{p} + \left(\zeta + \frac{4}{3}\eta\right)\boldsymbol{\nabla}(\boldsymbol{\nabla}\cdot\tilde{\mathbf{u}}) - \eta\boldsymbol{\nabla}\times(\boldsymbol{\nabla}\times\tilde{\mathbf{u}}), \tag{3}$$

the continuity equation

$$\frac{\partial\tilde{\rho}}{\partial t} + \rho\boldsymbol{\nabla}\cdot\tilde{\mathbf{u}} = 0, \tag{4}$$

and the diffusion equation for heat flow

$$\rho T\frac{\partial\tilde{s}}{\partial t} = \lambda_T\boldsymbol{\nabla}^2\tilde{T}. \tag{5}$$

In addition, there are thermodynamic relationships between the fluctuating pressure, density, temperature, and entropy fields. We have neglected the entropy generation due to viscous stress [8] in Eq. (5) because the u^2 dependence in this term leads to a nonlinear solution and amplitude dependent dissipation, which was not observed. We estimate that omission of this term is justified as long as the acoustic pressure is much less than 2×10^4 Pa at $\tau = 3\times 10^{-4}$. We estimate that the largest acoustic pressure at this temperature was $\sim$100 Pa, therefore the omission is easily justified for this work. At $\tau = 1\times 10^{-5}$, the acoustic pressure must be much less than 20 Pa to avoid these nonlinear effects. Our measurements show that the acoustic pressure at $\tau = 1\times 10^{-5}$ is less than 5 Pa.

Without further approximation to the system of equations, we derive in the Appendix the relationships between the fields for three possible wave modes: the propagating acoustic wave, the thermal wave (in the fluid and in the solid), and the shear wave. To do so, we separate $\tilde{\mathbf{u}}$ into two parts: a

divergence-free part $\tilde{\mathbf{u}}_{\mathrm{vor}}$ that makes up the shear (vorticity) wave and a curl-free part $\tilde{\mathbf{u}}_l$ that contributes to both the acoustic wave and the thermal wave. The scalar fields contribute to only the acoustic and thermal waves. We obtain relationships between the complex wave vectors and frequencies for these modes. We require only that the amplitudes of the oscillating temperature, density, and entropy be linear functions of the acoustic pressure. As long as this requirement is met, the solution is valid both near to and far from the critical point.

The solid wall is assumed to be rigid, nonporous, and smooth. Thermal expansion and sound propagation in the solid are ignored. Heat flow in the solid is governed by the diffusion equation

$$\lambda_{Ts}\boldsymbol{\nabla}^2\tilde{T}_s = \rho_s T_s \frac{\partial \tilde{s}_s}{\partial t} = i\omega\rho_s C_{Ps}\tilde{T}_s. \tag{6}$$

Therefore the solid supports a thermal wave characterized by the solid's effusivity $\varepsilon_s=(\rho_s C_{Ps}\lambda_{Ts})^{1/2}$ and thermal diffusivity $D_{Ts}=\lambda_{Ts}/(\rho_s C_{Ps})$, where ρ_s is the density, C_{Ps} is the specific heat per unit mass, and λ_{Ts} is the thermal conductivity. (Unless stated otherwise, the subscript s identifies a property of the solid.) The solid contains no heat sources, so heat can enter or leave the solid only through the boundary with the fluid. As in the fluid, the thermal wave in the solid vanishes exponentially with a characteristic thermal penetration length $\delta_{Ts}=(2D_{Ts}/\omega)^{1/2}$. The temperature and heat flow across the boundary are assumed to be continuous. These considerations lead to the boundary conditions on the fields at the wall:

$$|\tilde{\mathbf{u}}_\perp(0)| = 0 \text{ (rigid wall)}, \tag{7a}$$

$$|\tilde{\mathbf{u}}_\parallel(0)| = 0 \text{ (no slip)}, \tag{7b}$$

$$\tilde{T}(0) = \tilde{T}_s(0) \text{ (local equilibrium)}, \tag{7c}$$

$$[\lambda_T \boldsymbol{\nabla}_\perp \tilde{T}(0)] = [\lambda_T \boldsymbol{\nabla}_\perp \tilde{T}(0)]_s \text{ (energy conservation)}. \tag{7d}$$

The subscripts $\perp$ and $\parallel$ designate, respectively, the components perpendicular and parallel to the wall. The notations $\tilde{T}(0)$ and $\boldsymbol{\nabla}\tilde{T}(0)$ stand for, respectively, the temperature $\tilde{T}$ and the gradient of $\tilde{T}$ evaluated at the boundary.

As shown in the Appendix, the thermal boundary layer thickness δ_T comes naturally out of the fourth order differential equation for the acoustic fields, shown for the temperature as Eq. (A2), in terms of the dimensionless wave vector q_+, i.e.,

$$\delta_T^2 = -\frac{c^2}{\omega^2}\frac{2i}{q_+^2} \approx \frac{2D_T}{\omega}\frac{1+i\gamma\Delta_v}{1+i\Delta_v} \tag{8}$$

where $\Delta_v \equiv (\omega/c^2)\left(\zeta+\frac{4}{3}\eta\right)/\rho$. Far above T_c where Δ_v is very small, δ_T is real and has the physical interpretation as the distance heat will diffuse during an acoustic cycle. As the temperature is lowered toward T_c on the critical isochore, the value of D_T drops and, initially, so does δ_T. However, ζ and γ grow rapidly as $\tau\to 0$ and eventually dominate. Thus δ_T becomes complex and its magnitude passes through a minimum, signifying the transition between the "classical" and "viscous" regimes described by Carlés [3]. The minimum of $|\delta_T|$ occurs when $\gamma\Delta_v \approx 0.5$, and it coincides with the appearance of a non-negligible thermal wave pressure $\tilde{p}_T$ within the boundary layer. The magnitude of $\tilde{p}_T$ is limited by the thermal effusivity of the wall.

From the requirement that the temperature and the heat flow are continuous across the fluid-solid boundary, we find that the relationship between the thermal wave amplitudes in the solid and fluid involves the ratio of the effusivities of the two media, $\varepsilon/\varepsilon_s$. Far from the critical point, this ratio is very small and the resonator wall is very nearly isothermal. As T_c is approached along the critical isochore, $\varepsilon/\varepsilon_s$ increases as $(C_P\lambda_T)^{1/2}\propto\tau^{-0.8}$ (-0.8 is an effective exponent) and eventually becomes much larger than 1. We define the reduced temperature τ_ϑ as the value of τ where $\varepsilon=\varepsilon_s$; thus τ_ϑ depends on the effusivity of the solid.

For a standing wave in an acoustic resonator, we define the resonance quality factor Q as 2π (total acoustic energy)/(energy lost per cycle). The fractional energy lost per cycle Q^{-1} is

$$Q^{-1} = \frac{\frac{1}{\omega}\int_V \langle \dot{\mathsf{E}}\rangle_t dV}{\int_V [\langle E_P\rangle_t + \langle E_K\rangle_t] dV}, \tag{9}$$

where $\dot{\mathsf{E}}$ is the rate of energy loss per unit volume, E_P and E_K denote acoustic potential and kinetic energies per unit volume, respectively, and the angle brackets denote a time average. From the fields that satisfy Eqs. (3)–(6) and the boundary conditions (7), the time-averaged rate of energy loss per unit volume [7] is

$$\langle \dot{\mathsf{E}}\rangle_t = -\frac{1}{2}\mathrm{Re}\,[\boldsymbol{\nabla}\cdot(\tilde{p}^*\tilde{\mathbf{u}})] = -\frac{\omega}{2\rho}\mathrm{Im}[\tilde{p}^*\tilde{\rho}] - \frac{1}{2}\mathrm{Re}[(\boldsymbol{\nabla}\tilde{p}^*)\cdot\tilde{\mathbf{u}}], \tag{10}$$

where the asterisk denotes complex conjugation. The time-averaged acoustic potential and kinetic energies per unit volume are, respectively,

$$\langle E_P\rangle_t = \frac{1}{4\rho}\mathrm{Re}[\tilde{p}^*\tilde{\rho}] \tag{11}$$

and

$$\langle E_K\rangle_t = \left\langle \frac{1}{2}\rho\tilde{\mathbf{u}}\cdot\tilde{\mathbf{u}} \right\rangle_t = \frac{1}{4}\rho|\tilde{\mathbf{u}}|^2. \tag{12}$$

In the steady state, the time-averaged potential and kinetic energies are equal, so Eq. (9) becomes

$$Q^{-1} = Q_v^{-1} + Q_T^{-1}, \tag{13}$$

where

$$Q_v^{-1} = -\frac{1}{\rho\omega}\frac{\int_V \mathrm{Re}[(\nabla\tilde{p}^*)\cdot\tilde{\mathbf{u}}]dV}{\int_V |\tilde{\mathbf{u}}|^2 dV} \tag{14}$$

and

$$Q_T^{-1} = -\frac{\int_V \mathrm{Im}[\tilde{p}^*\tilde{\rho}]dV}{\int_V \mathrm{Re}[\tilde{p}^*\tilde{\rho}]dV}. \tag{15}$$

Q_v^{-1} represents predominantly viscous dissipation, and Q_T^{-1} represents predominantly thermal dissipation. Volume and surface processes contribute to both Q_v^{-1} and Q_T^{-1}.

Equations (14) and (15) show how the dissipation depends on the phase relationships between $\tilde{p}$, $\tilde{\rho}$, and $\tilde{\mathbf{u}}$. When $\tilde{\rho}$ and $\tilde{p}$ are in phase, the quantity $\tilde{p}^*\tilde{\rho}$ has no imaginary part and there is no thermal dissipation. Equation (15) can also be written in terms of the compressibility $\kappa \equiv \tilde{\rho}/(\rho\tilde{p})$,

$$Q_T^{-1} = -\frac{\int_V |\tilde{p}|^2 \mathrm{Im}[\kappa]dV}{\int_V |\tilde{p}|^2 \mathrm{Re}[\kappa]dV}. \tag{16}$$

When the conditions $\gamma\omega D_T/c^2 \ll 1$ and $\gamma\omega D_v/c^2 \ll 1$ are satisfied, i.e., not too close to the critical point, the compressibility is

$$\kappa \approx \kappa_S\left[1 + \frac{\gamma-1}{1+\vartheta}e^{-(1+i)x/\delta_T}\right], \tag{17}$$

where $\vartheta \approx \varepsilon/\varepsilon_s$. [Equation (A28) in the Appendix is the exact expression for ϑ.] Equation (17) reduces to the adiabatic compressibility κ_S far from the wall ($x \to \infty$). (Note that κ equals the isothermal compressibility $\kappa_T = \gamma\kappa_S$ at $x=0$ for a perfect wall [8].) In this level of approximation, the corresponding dissipation terms become

$$Q_v^{-1} \approx \frac{\delta_v}{2}\frac{\oint_S |\tilde{\mathbf{u}}_\parallel|^2 dS}{\int_V |\tilde{\mathbf{u}}|^2 dV} + \frac{\omega}{c^2}\left(\frac{\zeta}{\rho} + \frac{4}{3}D_v\right) + \mathrm{O}(\delta^2) \tag{18}$$

and

$$Q_T^{-1} \approx \frac{\delta_T}{2}\frac{\gamma-1}{1+\vartheta}\frac{\oint_S |\tilde{p}|^2 dS}{\int_V |\tilde{p}|^2 dV} + (\gamma-1)\frac{\omega}{c^2}D_T + \mathrm{O}(\delta^2). \tag{19}$$

The leading terms in Eqs. (18) and (19) are denoted Q_η^{-1} and Q_λ^{-1} because they come from the surface viscous and thermal dissipation, respectively. The lowest order contributions to the volume dissipation (the second terms) have been separated out from the other high order terms. In general, the separation of the dissipation into surface and volume terms is an approximation; the separation of the thermal and viscous dissipation is an additional approximation. These separations are useful for designing the experiments and for interpreting the qualitative features of the results.

At the frequencies we use, the volume dissipation from shear viscosity and thermal conduction is negligible. [In xenon at $\tau = 1\times10^{-6}$ and 10 kHz, the volume dissipation from shear viscosity $(4/3)(\omega/c^2)D_v$ is $\approx 2\times10^{-6}$ and the volume dissipation from thermal conduction $(\gamma-1)(\omega/c^2)D_T$ is $\approx 5\times10^{-5}$.] However, the leading volume dissipation term that depends on the bulk viscosity,

$$Q_\zeta^{-1} \approx \frac{\omega\zeta}{\rho c^2}, \tag{20}$$

is important; this term is ≈ 0.1 at $\tau = 1\times10^{-6}$ and 10 kHz. Because this paper focuses on the boundary layers, the analysis in Sec. IV is restricted to the data for which Q_ζ^{-1} is less than 0.8% of the total dissipation.

The expressions for the dissipation, Eqs. (18) and (19), are familiar [2,12] except for the factor $(1+\vartheta)$ in Eq. (19). Far from the liquid-vapor critical point, the energy content per unit area within the thermal boundary layer of the gas is much smaller than that in the solid, i.e., $\vartheta \ll 1$; then, $(1+\vartheta) \approx 1$, and the usual expression is recovered. The ratios of integrals in Eqs. (18) and (19) are geometric factors that can be calculated analytically for resonators with a high degree of symmetry [2,12]. The integral ratios for the more complicated resonator used in this work were estimated from numerical computations [13] and then adjusted slightly (±2%) to improve the agreement between the measurements far from T_c and theory. We replace the integral ratios in Eqs. (18) and (19) with $2q_v$ and $2q_T$, respectively, and write Q_η^{-1} and Q_λ^{-1} as

$$Q_\eta^{-1} \approx q_v\delta_v \tag{21}$$

$$Q_\lambda^{-1} \approx (\gamma-1)\frac{q_T\delta_T}{1+\vartheta}. \tag{22}$$

Figure 2 shows plots of Q_λ^{-1} for the Helmholtz mode of our resonator for two wall materials: bare stainless steel and a polymer coating. The solid curve in Fig. 2 shows Q_λ^{-1} for an idealized resonator that has walls with an infinite thermal conductivity. The dotted line in Fig. 2 shows the viscous dissipation Q_η^{-1} for the Helmholtz mode in both the steel and the polymer-coated resonators. The crosses in Fig. 2 indicate the reduced temperature where $\vartheta = 1$. The reduced temperature τ_ϑ separates two regimes. For $\tau > \tau_\vartheta$, the temperature gradient near the fluid-solid boundary occurs mostly in the fluid; for $\tau < \tau_\vartheta$, the temperature gradient occurs mostly in the solid, where the thermophysical properties are independent of τ. Equation (22) predicts that for $\tau \ll \tau_\vartheta$ the thermal dissipation is approximately

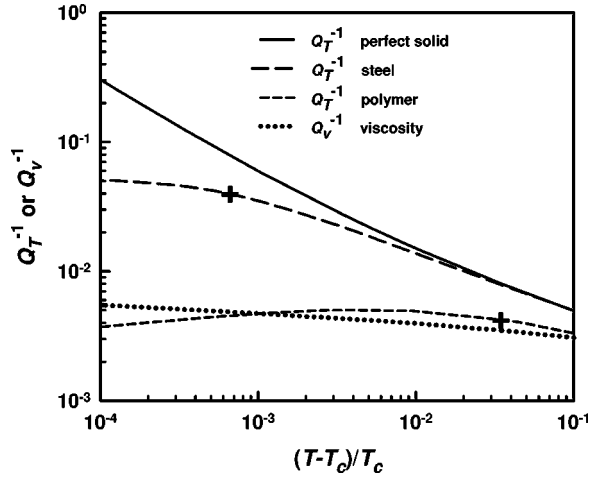

FIG. 2. Predicted thermal boundary dissipation as a function of reduced temperature in resonators made from stainless steel, a polymer, and a perfect solid. The crosses indicate where $\vartheta=1$. The viscous boundary dissipation is also shown for comparison.

$$Q_\lambda^{-1} \approx \sqrt{\frac{2}{k_{ac}}} \frac{q_T \varepsilon_s}{(\rho C_V \sqrt{c})}. \tag{23}$$

In the asymptotic critical regime, $\tau \ll 1$ and $Q_\lambda^{-1} \propto \tau^{0.08}$. Therefore a maximum occurs in Q_λ^{-1} near τ_ϑ. Solids with smaller effusivity have larger values of τ_ϑ and smaller maxima in Q_λ^{-1}.

III. ACOUSTIC ATTENUATION MEASUREMENTS

A. Resonator

The double-Helmholtz resonator shown in Fig. 1 was designed to be compact and to have several widely spaced, low-frequency, non degenerate modes. Widely spaced modes are needed to accurately measure the frequency dependence of the speed of sound and the attenuation of sound in near-critical fluids. Degenerate modes must be avoided because small imperfections of the resonator's shape or small intermode couplings will partially remove the degeneracy and yield a frequency response composed of partially overlapping peaks. Fits to overlapping peaks require many highly correlated parameters; the correlations increase the uncertainty of the Q's determined by fitting such modes.

We mention four design features of the resonator in Fig. 1. (i) The resonator is deliberately asymmetric, i.e., the two cylindrical chambers have equal volumes; however, their length-to-diameter ratios differ. Because of this, the longitudinal modes of the longer chamber are not degenerate with modes in the shorter chamber. In this work we studied the five lowest-frequency longitudinal modes of the longer chamber as well as the Helmholtz mode. These modes had nominal wave numbers $\omega/c=12$, 65, 130, 197, 261, and 326 m^{-1}. (ii) The two chambers are oriented at right angles to each other to keep the resonator compact. (iii) The chambers and the tube connecting them are machined from a single piece of metal to make a rigid, seamless structure. The rigidity reduces the deformation of the resonator (and its associated energy dissipation) in reaction to the oscillating xenon. By avoiding seams, we reduce the chance of energy dissipation in crevices. (iv) Thick (2.5 mm) diaphragms are used to transmit sound into and out of the resonator. These robust diaphragms withstand a differential pressure of 10 MPa, thereby eliminating the need for a pressure vessel.

Two identical resonators were made for this study. Both resonators were machined from type-316 stainless steel. The interior surfaces of both resonators were polished to a mirror finish to ensure that their effective areas were independent of the length scale set by the thermal penetration length in the xenon ($0.5 < \delta_T < 10$ μm). The polishing removed tool marks and scratches with a series of grits; the smallest grit was 0.5 μm.

The inner surface of one resonator was left bare. The inner surface of the other resonator was coated with an 80 -μm-thick layer of poly-monochloro-para-xylylene, a polymer known commercially as Parylene C [14]. The rms roughness of the polymer surface was less than 0.08 μm as determined with atomic force microscopy for length scales up to 80 μm. The ratio of the topographic surface area to the projected area was 1.0089 for areas between 3 and 2300 μm^2.

We chose this polymer as the coating material because it has a low effusivity, it is chemically stable, and because it adheres well to metal substrates. The polymer was deposited from its vapor. The deposition process creates a nonporous conformal film (no shadowing) and does not leave a solvent residue that might contaminate the xenon. The thickness of the polymer coating was estimated from micrometer measurements and from mass measurements of samples that were deposited when the resonator was coated. The estimated polymer thickness was $(85 \pm 15)\mu$m. Using the thermophysical properties supplied by the manufacturer, we estimated the effusivity of the polymer to be 277 kg K^{-1} $s^{-5/2}$. The effusivity that best fits our data is 370 kg K^{-1} $s^{-5/2}$. Using the manufacturer's data, we estimate the thermal penetration length in the polymer $\delta_{Ts}=17$ μm at 100 Hz. Therefore the polymer thickness was $4.9\delta_{Ts}$. We calculated the thermal boundary dissipation when the xenon is in contact with a layer of one solid on a semi-infinite slab of another solid. If the layer is at least $5\delta_{Ts}$ thick, the thermal dissipation is within 1% of that for an infinitely thick layer.

The two resonators were filled and studied in identical ways but not simultaneously. One resonator at a time was mounted inside a multishelled thermostat that had been used to test a previous microgravity experiment (Critical Viscosity of Xenon, CVX) [15]. The performance of the thermostat has been described in a previous publication [16]. The resonator's temperature was measured with a thermistor located in a machined well in the resonator's body. The thermistor was calibrated against an industrial platinum resistance thermometer that itself had drifted by 15 mK since it was last calibrated on ITS-90. We used 15 mK as the combined standard uncertainty of the thermistor's calibration.

A 0.5-mm-i.d. copper tube was vacuum brazed to a port in the resonator, through which gas could be removed or added with ease. The other end of the copper tube was attached to a small gas handling system through a high-pressure valve. The gas-handling system consisted of a pressure gauge, a gas

storage vessel, and a leak detector connected by small-diameter stainless steel tubing. With the valve closed, the evacuated or filled resonator could be detached from the manifold and weighed. Once the resonator was filled with xenon to the critical density, the tube was crimped over a 1 -cm length, cut, and then brazed to permanently seal the xenon inside.

B. Sample density and purity

The xenon's density was determined from mass and volume measurements. We measured the combined volume of the resonator, the fill tube, and the valve by a gas expansion technique. We filled a known volume with argon gas and measured its initial temperature and pressure. After successive expansions of the argon from the known volume to the manifold and then to the resonator, we again measured the temperature and pressure. We determined the argon's density from an equation of state [17] after each expansion. The uncertainty in argon's density was 0.02%. The volume of the bare stainless steel resonator, its fill tube, and valve was (19.501 ± 0.004) cm^3. For the polymer-coated resonator, the combined volume was (18.822 ± 0.007) cm^3.

After the mass of the empty resonator was measured, we added enough xenon to overfill the resonator by approximately 5%. The amount of xenon added was estimated from the change in pressure of the storage vessel. Then the resonator was placed back on the balance and small amounts of xenon were released until the desired mass of xenon was left in the resonator. The bare stainless steel resonator was filled with (21.757 ± 0.002) g of xenon at a density of (1115.7 ± 0.2) kg m^{-3}. The polymer-coated resonator was filled with (21.006 ± 0.002) g of xenon at a density of (1116.0 ± 0.4) kg m^{-3}.

The manufacturer (Matheson Gas Products [14]) stated that the xenon was 99.995% pure. No additional analysis or purification was performed.

C. Acoustic transducers

The thick diaphragms mentioned above were machined into flanges that formed the ends of the cylindrically shaped chambers. The flanges were sealed to the resonator body with gold wire o-rings and high-strength alloy screws. Thin piezoceramic disks were firmly cemented to the outside surface of each diaphragm. These transducers generated and detected sound. The polarization for these disks was oriented perpendicular to the electrodes, which were bonded to the flat faces. The voltage across the electrodes was coupled to the acoustic pressure in the gas through stresses and strains in the piezoceramic material caused by the flexure of the diaphragm.

The three piezoceramic transducers attached to the diaphragms were identical. A transducer at one end of the long chamber was used as the sound source. A transducer at the other end of the long chamber was the detector. The same pair of transducers was used to drive and detect all the modes. The third transducer at the end of the short chamber was used only for diagnostic purposes. A digital function generator drove the source transducer with a sinusoidal voltage at frequency f, and it provided the reference signal for a digital, two-phase lock-in amplifier. The lock-in amplifier measured the in-phase and quadrature signals, also at f, from the detector. For each acoustic mode we studied, the drive and detector voltages were measured at 11 frequencies spanning the full width of the resonance. The frequency was scanned upward and downward to remove the effects of a linear temperature drift. The measured signal was averaged for 2 sec at each frequency to improve the signal to noise ratio. A computer controlled the data acquisition.

When the piezoceramic source transducer was excited with 7 V (rms), it generated a volume displacement δV_c in the chamber of approximately $1 \times 10^{-7}\ V_c$, where V_c is the volume of one chamber. This volume displacement did not vary by more than 10% between 100 Hz and 6 kHz. The diaphragm's sinusoidal volume displacement generated a pressure wave in the gas. The acoustic pressure at the resonance frequency of the Helmholtz mode f_H was $Q\rho c^2 \delta V_c/(2V_c)$. For the longitudinal modes, the acoustic pressure was $2Q\rho c^2 \delta V_c/V_c$.

We determined the acoustic pressure from the detector signal using a model for the electro-acoustic response of the thick diaphragms and piezoceramic transducers. The model yielded a detector sensitivity of 6 μV/Pa for all the modes. For the 7-V source excitation, the acoustic pressure at f_H ranged from 100 Pa at the highest temperature ($\tau = 4 \times 10^{-2}$) to 9 Pa at the lowest temperature ($\tau = 3 \times 10^{-4}$). For the same excitation voltage, the acoustic pressure of the longitudinal modes was approximately ten times higher than that of the Helmholtz mode because the longitudinal resonances had higher Q's and because the coupling to the longitudinal modes was four times more efficient.

Precautions were taken to avoid nonlinear dependence on the drive level. The acoustic pressure amplitudes in all our measurements were small enough to avoid hydrodynamic nonlinearities. If the temperature oscillation is too large very close to the critical point, then the average of the singular thermodynamic properties over the acoustic cycle will differ from the values at the average temperature and the true critical behavior will not be observed. This limit on the temperature oscillation places a stricter limit on the pressure amplitude than hydrodynamic linearity. An acoustic pressure of 60 Pa will result in a 1% error in the bulk viscosity at $\tau = 3 \times 10^{-4}$, whereas 90 Pa is required to cause a 1% error in C_P. If nonlinear hydrodynamics or nonlinear averaging had been important, then the measured resonance line shape would have depended on the drive level. For all the modes we studied, a ten fold reduction in the drive level did not measurably affect the Q. Also, we verified that the power dissipated in the drive transducer did not heat the resonator significantly.

D. Determination of the critical temperature

To determine the critical temperature T_c of the xenon in each resonator, we measured the resonance frequency of the Helmholtz mode $f_H(T)$ as a function of the temperature. In the approximation that f_H is proportional to the thermodynamic speed of sound (i.e., the zero-frequency speed of

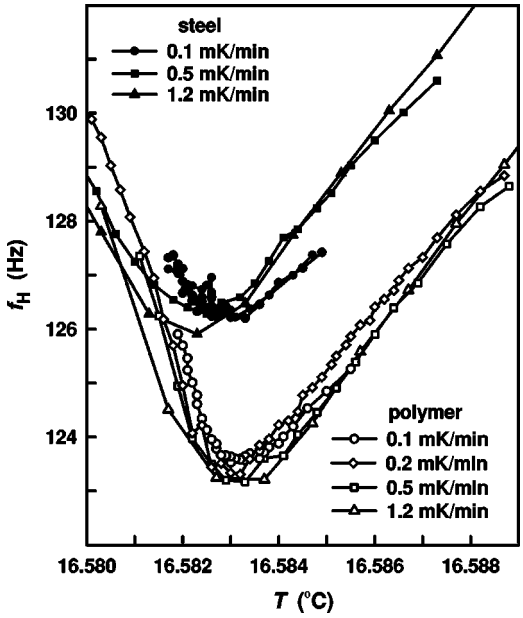

FIG. 3. The Helmholtz mode resonance frequency f_H plotted as a function of temperature for different temperature ramp rates. The temperatures of the minima were used to determine T_c.

sound) in xenon at its critical density, the theory of critical phenomena predicts $f_H(T)$ varies as $\tau^{\alpha/2}$ (with $\alpha=0.110$), and therefore vanishes with a cusp at the critical point. We consider first the effects of the earth's gravity and then the effect of nonzero frequency.

Under the earth's gravity, near-critical xenon compresses under its own weight and forms a vertically stratified sample such that the density equals ρ_c at only one height. (This height is midway between the top and bottom of the resonator, if the average density of the xenon is ρ_c.) In equilibrium, the frequency of the Helmholtz mode $f_H(T)$ is determined by suitably averaging the speed of sound over the stratified sample. We calculated the averaged values of $f_H(T)$ by solving numerically the wave equation in stratified xenon with a rectangular cross section 23.5 mm high. In this model, $f_H(T)$ does not vanish at T_c; instead, $f_H(T)$ has a shallow minimum approximately 15 mK above T_c. In principle, we could have fit $f_H(T)$ to a refined model that accounts for the actual cross section of the resonant cavities. However, the result would still be uncertain because of our limited knowledge of the equation of state of xenon. Instead, we chose to stir the xenon to reduce the effect of gravity on $f_H(T)$. We recognize that a fully stirred sample is not in thermal equilibrium. From considerations in Ref. [18], stirring replaces the isothermal density profile with an adiabatic density profile. The isothermal profile is sigmoidal and spans the density range $\Delta\rho \approx \pm 0.07\rho_c$. The adiabatic profile is nearly linear in temperature ($dT/dz \approx -1$ mK cm^{-1}) and density and spans the very small density range $\Delta\rho \approx \pm 5\times10^{-5}\rho_c$. In the adiabatically stratified xenon, $f_H(T)$ has a much deeper minimum that is within ±1 mK of T_c for our 23.5-mm high sample.

To stir the xenon, we ramped the temperature of the thermostat downward. The ramping created small temperature gradients in the xenon that drove convection. Before each ramp, the resonator was warmed 0.42 K above T_c and allowed to equilibrate. Then the temperature was lowered (in 10–30 min) to just above T_c, and the ramp was begun. The data in Fig. 3 show that consistent results were obtained for the Helmholtz frequency $f_H(T)$ with ramp rates spanning a factor of 10. At still faster ramp rates, the temperature of the xenon lags behind the thermometer installed in the side of the resonator. At slower ramp rates, evidence of stratification was found.

We determined the precise location of the minima by fitting $f_H(T)$ to a quadratic polynomial. For the polymer-coated resonator, we observed the minimum at 16.5833°C (standard deviation 0.0001°C) with four ramp rates 0.1, 0.2, 0.5, and 1.2 mK min^{-1}. For the same range of ramp rates in the bare steel resonator, the average location of the minima was 16.5828°C (standard deviation 0.0004°C). Based on these measurements, we chose $T_c=16.583$°C for both resonators. The uncertainty of T_c must be at least ±1 mK due to the adiabatic temperature gradient in the convectively stirred xenon as discussed above. Although these values of T_c are mutually consistent, they might differ from each other by as much as 2 mK; we have detected 2-mK changes when the

TABLE I. Results for the Helmholtz mode in the bare steel resonator. The resonance frequency f_r and half width g_r were from fits of Eq. (24) to the acoustic data and corrected according to Eqs. (25) and (26) as discussed in the text. The speed of sound $c_{\rm HS}$ was determined from the acoustic data, k_0 from a calibration with argon, and Eq. (29). The fractional deviations of $Q_r^{-1}=2g_r/f_r$ from the model, where $\Delta Q^{-1}/Q^{-1} \equiv (Q_r^{-1}-Q_{\rm mod}^{-1})/Q_{\rm mod}^{-1}$.

T(°C)	τ	f_r(Hz)	g_r(Hz)	$c_{\rm HS}$(m s^{-1})	$\Delta Q^{-1}/Q^{-1}$
16.683[a]	3.48×10^{-4}	161.7581	4.3963	84.942	
16.704[a]	4.20×10^{-4}	164.7404	4.3307	86.422	
16.732[a]	5.18×10^{-4}	168.1319	4.2189	88.084	
16.767	6.39×10^{-4}	171.7045	4.1167	89.842	3.34×10^{-4}
16.810	7.88×10^{-4}	175.4707	3.9691	91.676	1.13×10^{-3}
16.864	9.72×10^{-4}	179.3597	3.8050	93.564	1.69×10^{-3}
16.939	1.23×10^{-3}	183.9478	3.6019	95.787	7.51×10^{-4}
17.023	1.52×10^{-3}	188.1982	3.4194	97.851	9.69×10^{-4}
17.125	1.88×10^{-3}	192.6129	3.2303	99.996	1.14×10^{-4}
17.252	2.31×10^{-3}	197.2016	3.0411	102.231	-1.04×10^{-3}
17.409	2.85×10^{-3}	201.9735	2.8629	104.566	2.02×10^{-4}
17.602	3.52×10^{-3}	206.9397	2.6839	107.001	-9.28×10^{-4}
17.841	4.35×10^{-3}	212.1077	2.5142	109.545	-1.72×10^{-3}
18.135	5.36×10^{-3}	217.5125	2.3580	112.217	-1.06×10^{-3}
18.498	6.61×10^{-3}	223.1647	2.2106	115.021	-1.12×10^{-3}
18.946	8.16×10^{-3}	229.0934	2.0748	117.973	-9.30×10^{-4}
19.498	1.01×10^{-2}	235.3336	1.9508	121.090	-4.57×10^{-4}
20.179	1.24×10^{-2}	241.9257	1.8378	124.394	-7.18×10^{-5}
21.020	1.53×10^{-2}	248.9156	1.7363	127.906	6.79×10^{-4}
22.057	1.89×10^{-2}	256.3622	1.6436	131.657	4.89×10^{-4}
23.337	2.33×10^{-2}	264.3278	1.5609	135.677	3.98×10^{-4}
24.915	2.88×10^{-2}	272.8887	1.4880	140.007	5.90×10^{-4}
26.862	3.55×10^{-2}	282.1399	1.4232	144.693	4.78×10^{-4}

[a]Point omitted from the analysis.

TABLE II. Results for the second longitudinal mode in the bare steel resonator. The resonance frequency f_r and half width g_r were from fits of Eq. (24) to the acoustic data and corrected according to Eqs. (25) and (26) as discussed in the text. The speed of sound c_{L2} was determined from the acoustic data, k_0 from a calibration to c_{HS} at one temperature, and Eq. (39). The fractional deviations of $Q_r^{-1} = 2g_r/f_r$ from the model, where $\Delta Q^{-1}/Q^{-1} \equiv (Q_r^{-1} - Q_{\mathrm{mod}}^{-1})/Q_{\mathrm{mod}}^{-1}$.

T(°C)	τ	f_r(Hz)	g_r(Hz)	c_{L2}(m s^{-1})	$\Delta Q^{-1}/Q^{-1}$
16.683[a]	3.48×10^{-4}	1733.633	19.463		
16.704[a]	4.20×10^{-4}	1764.795	17.990		
16.732[a]	5.18×10^{-4}	1799.779	16.721		
16.767[a]	6.39×10^{-4}	1836.791	15.649		
16.810[a]	7.88×10^{-4}	1875.291	14.729		
16.864[a]	9.72×10^{-4}	1915.326	13.890		
16.939[a]	1.23×10^{-3}	1962.158	12.999		
17.023[a]	1.52×10^{-3}	2005.206	12.237		
17.125[a]	1.88×10^{-3}	2050.330	11.474		
17.252[a]	2.31×10^{-3}	2097.320	10.723		
17.409[a]	2.85×10^{-3}	2146.184	9.995		
17.602[a]	3.52×10^{-3}	2197.195	9.289		
17.841	4.35×10^{-3}	2250.418	8.617	109.547	-6.75×10^{-3}
18.135	5.36×10^{-3}	2306.108	7.979	112.217	-4.44×10^{-3}
18.498	6.61×10^{-3}	2364.537	7.383	115.021	-2.52×10^{-3}
18.946	8.16×10^{-3}	2425.968	6.828	117.973	-1.28×10^{-3}
19.498	1.01×10^{-2}	2490.765	6.318	121.090	-3.65×10^{-4}
20.179	1.24×10^{-2}	2559.332	5.851	124.393	8.08×10^{-5}
21.020	1.53×10^{-2}	2632.182	5.424	127.904	-1.23×10^{-4}
22.057	1.89×10^{-2}	2709.899	5.036	131.654	-6.84×10^{-4}
23.337	2.33×10^{-2}	2793.154	4.684	135.674	-1.83×10^{-3}
24.915	2.88×10^{-2}	2882.739	4.367	140.003	-3.47×10^{-3}
26.862	3.55×10^{-2}	2979.643	4.081	144.688	-5.70×10^{-3}

[a]Point omitted from the analysis.

TABLE III. Results for the fifth longitudinal mode in the bare steel resonator. The resonance frequency f_r and half width g_r were from fits of Eq. (24) to the acoustic data and corrected according to Eqs. (25) and (26) as discussed in the text. The speed of sound c_{L5} was determined from the acoustic data, k_0 from a calibration to c_{HS} at one temperature, and Eq. (39). The fractional deviations of $Q_r^{-1} = 2g_r/f_r$ from the model, where $\Delta Q^{-1}/Q^{-1} \equiv (Q_r^{-1} - Q_{\mathrm{mod}}^{-1})/Q_{\mathrm{mod}}^{-1}$.

T(°C)	τ	f_r(Hz)	g_r(Hz)	c_{L5}(m s^{-1})	$\Delta Q^{-1}/Q^{-1}$
16.683[a]	3.48×10^{-4}	4380.179	50.153		
16.704[a]	4.20×10^{-4}	4455.946	42.840		
16.732[a]	5.18×10^{-4}	4543.372	36.415		
16.767[a]	6.39×10^{-4}	4635.958	31.379		
16.810[a]	7.88×10^{-4}	4732.200	27.484		
16.864[a]	9.72×10^{-4}	4832.780	24.433		
16.939[a]	1.23×10^{-3}	4950.850	21.731		
17.023[a]	1.52×10^{-3}	5060.094	19.785		
17.125[a]	1.88×10^{-3}	5173.121	18.122		
17.252[a]	2.31×10^{-3}	5290.882	16.654		
17.409[a]	2.85×10^{-3}	5413.339	15.345		
17.602[a]	3.52×10^{-3}	5541.155	14.140		
17.841[a]	4.35×10^{-3}	5674.598	13.043		
18.135[a]	5.36×10^{-3}	5814.284	12.034		
18.498[a]	6.61×10^{-3}	5960.866	11.106		
18.946[a]	8.16×10^{-3}	6115.000	10.257		
19.498[a]	1.01×10^{-2}	6277.669	9.481		
20.179[a]	1.24×10^{-2}	6449.880	8.775		
21.020	1.53×10^{-2}	6632.904	8.131	127.907	-1.24×10^{-3}
22.057	1.89×10^{-2}	6828.219	7.547	131.658	-6.25×10^{-4}
23.337	2.33×10^{-2}	7037.521	7.019	135.679	-6.07×10^{-4}
24.915	2.88×10^{-2}	7262.794	6.538	140.009	-1.91×10^{-3}
26.862	3.55×10^{-2}	7506.531	6.103	144.695	-4.25×10^{-3}

[a]Point omitted from the analysis.

thermistor was removed from one resonator and replaced at a later time. Furthermore, both values of T_c might differ from ITS-90 by as much as 15 mK, the uncertainty of the thermometer used to calibrate the thermistor.

We were concerned that the value of T_c determined from $f_H(T)$ in the stirred sample might depend upon the acoustic frequency. However, we found precisely the same value of T_c by measuring the frequency of the first longitudinal mode $f_{L1}(T)$ in the stirred fluid using the procedure described above. (Note: $f_{L1}/f_H \approx 5$.)

IV. DATA ANALYSIS

We fit the in-phase and quadrature components of the detector voltage with a standard acoustic resonance formula [10],

$$u + iv = \frac{Af}{F_r^2 - f^2} + B + C(f - \overline{f}). \tag{24}$$

The complex parameters A, B, C, and F_r were adjusted to minimize the squared deviations of Eq. (24) from the data. Thus a total of eight independent parameters were adjusted for each resonance. From this fit, we obtain the resonance frequency $f_r = \mathrm{Re}(F_r)$ and half width $g_r = \mathrm{Im}(F_r)$. The constant $\overline{f}$ is not adjusted, but it is fixed midway between the maximum and minimum frequency of the data set.

The fractional rms deviations from the fits with Eq. (24) were at most 0.001, corresponding to an uncertainty from random noise of $0.001g_r$ for both f_r and g_r. After an initial analysis, we discovered that fits with Eq. (24) introduce systematic errors that grow as Q decreases. The errors arise because the standard resonance formula ignores the frequency dependence of the dissipation mechanisms that contribute to the half width ($g_r \propto f^{-1/2}$ for surface losses and $\propto f$ for volume losses). In effect, the half width itself is frequency dependent. We corrected these small systematic errors by fitting Eq. (24) to numerical data generated from a model that included the frequency dependent dissipation. The errors in the fitted resonance frequencies and Q's were described by the empirical expressions

$$\frac{f_{r,corr}-f_{r,fit}}{f_{r,fit}} = -\frac{1}{8}Q_{surf}^{-2}+\frac{1}{4}Q_{vol}^{-2}+\frac{1}{8}Q_{surf}^{-1}Q_{vol}^{-1}-\frac{1}{8}Q_{surf}^{-3}, \tag{25}$$

$$Q_{corr}^{-1}-Q_{fit}^{-1} = -\frac{1}{4}Q_{surf}^{-2}-(0.263)Q_{surf}^{-1}Q_{vol}^{-1}+\frac{1}{4}Q_{surf}^{-3}, \tag{26}$$

where Q_{surf}^{-1} and Q_{vol}^{-1} are the surface losses (viscous and thermal) and volume losses (bulk viscosity), respectively, in the vicinity of the resonance. Equations (25) and (26) were used, with Q_{surf}^{-1} and Q_{vol}^{-1} estimated from our acoustic model, to correct the fitted resonance frequencies and half widths for the measurements in xenon. The largest corrections were for the Helmholtz mode at the lowest temperature: $|\Delta f_r/f_r| \leqslant 0.04\%$ and $|\Delta Q^{-1}/Q^{-1}| \leqslant 1.5\%$.

Values of the corrected resonance frequencies and half widths for the Helmholtz mode and for the second and fifth longitudinal modes at selected temperatures are presented in Tables I–VI. Tables I–III contain the data for the bare stainless steel resonator. Tables IV–VI contain the data for the polymer-coated resonator.

A. Model of the Helmholtz mode

To relate the concepts developed in Sec. III to measurements in our Helmholtz resonator, consider the detailed acoustic model for the Greenspan viscometer [2]. Equation (25) in Ref. [2] gives the resonance condition for the Helmholtz mode when the fill duct is neglected. The sealed fill duct for our resonator was only 2 cm long with a 0.5-mm diameter, so gas flow in or out of the tube was negligible. Numerical calculations [13] showed that the fill duct would increase q_T by 0.7% and decrease the wave number by less than 0.04% for the Helmholtz mode. These small constant effects were accounted for in the calibration.

The complex resonance frequency of the Helmholtz mode is given to sufficient accuracy by

$$\left(\frac{F_H}{f_0}\right)^2 = \frac{1}{1+(1-i)(\gamma-1)\dfrac{q_T\delta_T}{1+\vartheta}} \times \frac{1+\dfrac{L_d}{L_d+2\delta_i}[G(ik_0L_d/2)-1]}{1+(1-i)q_v\delta_v+\dfrac{L_d}{L_d+2\delta_i}[G(\Gamma L_d/2)-1]\left[1+(1-i)\dfrac{\delta_v}{r_d}\right]}, \tag{27}$$

where $f_0=k_0c/(2\pi)$ would be the resonance frequency if there were no dissipation, r_d is the duct radius, and L_d is the duct length. The end correction δ_i, discussed in Ref. [2], is on the order of $0.7r_d$ here. We have defined the function $G(x)\equiv\tanh(x)/x$. The propagation parameter Γ is given by

$$\Gamma = \frac{i\omega}{c}\sqrt{\frac{1+\vartheta+(\gamma-1)F_T}{(1+\vartheta)(1-F_v)}} \tag{28}$$

with $F_T \approx (1-i)\delta_T/r_d$ and $F_v \approx (1-i)\delta_v/r_d$. Equations (27) and (28) have been modified from the expressions in Ref. [2] by the factor $(1+\vartheta)$ to account for the effusivity of the solid.

From a calculated or calibrated value for k_0, the speed of sound can be determined from the measured resonance frequency and half width with the expression

$$c_H = \frac{2\pi(f_r+g_r-g_b)}{k_0[\mathrm{Re}(F_H/f_0)+\mathrm{Im}(F_H/f_0)]}, \tag{29}$$

where the partial half width due to the bulk viscosity $g_b = f_rQ_\zeta^{-1}/2$ must be calculated. The total dissipation predicted from the model is then

$$Q_H^{-1} = \frac{2\ \mathrm{Im}(F_H)}{\mathrm{Re}(F_H)}+Q_\zeta^{-1}. \tag{30}$$

B. Derived xenon properties

1. Speed of sound

We used the measurements from the Helmholtz mode in the uncoated resonator to derive the properties of xenon because this mode was most affected by xenon's thermal conductivity and least affected by bulk viscosity. The value of k_0 for the Helmholtz mode was calibrated with argon gas before the resonator was filled with xenon. The calibrated value, 12.314 m^{-1}, was within 0.4% of the value calculated numerically for this geometry by Mehl [13] and within 0.6% of an estimate based on analytic formulations given in Ref. [2]. We used this calibration in Eq. (29) to determine the speed of sound c_{HS} in xenon at its critical density. The results for selected temperatures are plotted in Fig. 4(a) and listed in Table I.

Kline and Carome [19] measured the speed of sound in near critical xenon at 6 kHz a small resonant cavity. Their results are plotted in Fig. 4(a). Kline and Carome's measurements have a larger uncertainty than ours because they did not calibrate their resonator with a well-known gas nor did they correct the measured resonance frequencies for boundary layer perturbations. They report the uncertainty in their speed of sound to be 1% for $\tau > 10^{-3}$ and up to 2% for $\tau < 10^{-3}$. Our measurements agree within the scatter of their

TABLE IV. Results for the Helmholtz mode in the polymer-coated resonator. The resonance frequency f_r and half width g_r were from fits of Eq. (24) to the acoustic data and corrected according to Eqs. (25) and (26) as discussed in the text. The speed of sound c_H was determined from the acoustic data, k_0 from a calibration to c_{HS} at one temperature, and Eq. (29). The fractional deviations of $Q_r^{-1}=2g_r/f_r$ from the model, where $\Delta Q^{-1}/Q^{-1}\equiv(Q_r^{-1}-Q_{\mathrm{mod}}^{-1})/Q_{\mathrm{mod}}^{-1}$.

T(°C)	τ	f_r(Hz)	g_r(Hz)	c_{H}(m s^{-1})	$\Delta Q^{-1}/Q^{-1}$
16.683[a]	3.48×10^{-4}	159.779	1.015		
16.704[a]	4.20×10^{-4}	162.669	1.009		
16.732[a]	5.18×10^{-4}	165.994	1.005		
16.767[a]	6.39×10^{-4}	169.431	1.005		
16.810[a]	7.88×10^{-4}	172.989	1.008		
16.864	9.72×10^{-4}	176.674	1.015	93.410	3.39×10^{-4}
16.939	1.23×10^{-3}	180.993	1.022	95.684	1.76×10^{-4}
17.023	1.52×10^{-3}	184.959	1.029	97.773	4.47×10^{-4}
17.125	1.88×10^{-3}	189.086	1.036	99.947	1.68×10^{-4}
17.252	2.31×10^{-3}	193.375	1.045	102.206	6.93×10^{-4}
17.409	2.85×10^{-3}	197.832	1.051	104.552	-3.74×10^{-4}
17.602	3.52×10^{-3}	202.480	1.059	106.999	-4.27×10^{-4}
17.841	4.35×10^{-3}	207.329	1.065	109.552	-8.57×10^{-4}
18.135	5.36×10^{-3}	212.408	1.071	112.225	-6.86×10^{-4}
18.498	6.61×10^{-3}	217.736	1.076	115.028	-9.39×10^{-4}
18.946	8.16×10^{-3}	223.344	1.079	117.978	-1.08×10^{-3}
19.498	1.01×10^{-2}	229.262	1.081	121.090	-9.70×10^{-4}
20.179	1.24×10^{-2}	235.532	1.082	124.387	-9.50×10^{-4}
21.020	1.53×10^{-2}	242.199	1.081	127.891	-8.12×10^{-4}
22.057	1.89×10^{-2}	249.316	1.079	131.631	-8.00×10^{-4}
23.337	2.33×10^{-2}	256.948	1.076	135.641	-7.30×10^{-4}
24.915	2.88×10^{-2}	265.165	1.072	139.959	-3.61×10^{-4}
26.862	3.55×10^{-2}	274.051	1.068	144.628	-5.83×10^{-4}

[a]Point omitted from the analysis.

data (0.2%) far from T_c. Below $\tau=10^{-3}$, Kline and Carome's values are 2% higher than ours. This level of disagreement is not likely to be due to dispersion; it probably results from the criterion that Kline and Carome used to determine T_c. They assumed that the speed of sound averaged over an isothermal density profile has a minimum at T_c.

2. Heat capacity and thermal conductivity

We used our measured speed of sound c_{HS}, the isothermal susceptibility χ_T measured by Güttinger and Cannell [20], and $(\partial P/\partial T)_\rho$ from Swinney and Henry [21], to determine C_V and C_P with the equations

$$C_V=\frac{T\left(\frac{\partial P}{\partial T}\right)_\rho^2}{\rho^2\left[c_{\mathrm{HS}}^2-\frac{\rho}{\chi_T}\right]}, \tag{31}$$

TABLE V. Results for the second longitudinal mode in the polymer-coated resonator. The resonance frequency f_r and half width g_r were from fits of Eq. (24) to the acoustic data and corrected according to Eqs. (25) and (26) as discussed in the text. The speed of sound c_{L2} was determined from the acoustic data, k_0 from a calibration to c_{HS} at one temperature, and Eq. (39). The fractional deviations of $Q_r^{-1}=2g_r/f_r$ from the model, where $\Delta Q^{-1}/Q^{-1}\equiv(Q_r^{-1}-Q_{\mathrm{mod}}^{-1})/Q_{\mathrm{mod}}^{-1}$.

T(°C)	τ	f_r(Hz)	g_r(Hz)	c_{L2}(m s^{-1})	$\Delta Q^{-1}/Q^{-1}$
16.683[a]	3.48×10^{-4}	1743.635	9.048		
16.704[a]	4.20×10^{-4}	1774.991	7.524		
16.732[a]	5.18×10^{-4}	1811.048	6.246		
16.767[a]	6.39×10^{-4}	1848.482	5.310		
16.810[a]	7.88×10^{-4}	1887.358	4.648		
16.864[a]	9.72×10^{-4}	1927.542	4.180		
16.939[a]	1.23×10^{-3}	1974.667	3.816		
17.023[a]	1.52×10^{-3}	2017.916	3.599		
17.125[a]	1.88×10^{-3}	2062.915	3.448		
17.252[a]	2.31×10^{-3}	2109.643	3.343		
17.409[a]	2.85×10^{-3}	2158.181	3.268		
17.602[a]	3.52×10^{-3}	2208.805	3.215		
17.841[a]	4.35×10^{-3}	2261.613	3.174		
18.135[a]	5.36×10^{-3}	2316.890	3.141		
18.498[a]	6.61×10^{-3}	2374.871	3.110		
18.946[a]	8.16×10^{-3}	2435.866	3.079		
19.498	1.01×10^{-2}	2500.238	3.046	121.090	3.46×10^{-3}
20.179	1.24×10^{-2}	2568.417	3.010	124.387	4.03×10^{-3}
21.020	1.53×10^{-2}	2640.902	2.968	127.891	4.35×10^{-3}
22.057	1.89×10^{-2}	2718.275	2.922	131.632	4.33×10^{-3}
23.337	2.33×10^{-2}	2801.233	2.871	135.643	4.28×10^{-3}
24.915	2.88×10^{-2}	2890.551	2.816	139.960	3.95×10^{-3}
26.862	3.55×10^{-2}	2987.156	2.758	144.631	3.19×10^{-3}

[a]Point omitted from the analysis.

$$C_P=\frac{c_{\mathrm{HS}}^2\chi_T}{\rho}C_V, \tag{32}$$

where C_P and C_V are per unit mass quantities. The isothermal susceptibility χ_T is related to the isothermal compressibility κ_T by $\chi_T=\rho^2\kappa_T$. See Table VII for the functions, coefficients, and exponents used to calculate χ_T, $(\partial P/\partial T)_\rho$, and other quantities.

The largest uncertainty in our values of C_V comes from the derivative $(\partial P/\partial T)_\rho$. From a scaled equation of state, the dimensionless derivative $(\partial P^*/\partial T^*)_\rho\equiv(T_c/P_c)(\partial P/\partial T)_\rho$ has the form [21]

$$\left(\frac{\partial P^*}{\partial T^*}\right)_\rho=C_1+(2-\alpha)P_1^\pm|\tau|^{1-\alpha}+(3-2\alpha-2\beta)\rho_c H_2^\pm|\tau|^{2-2\alpha-2\beta}, \tag{33}$$

where C_1, $P_1^\pm$, and $H_2^\pm$ are constants, and the superscript $\pm$ distinguishes the constants for $\tau>0(+)$ and $\tau<0(-)$. In Ref. [21] the value $C_1=5.9253$ was determined from PVT data in

TABLE VI. Results for the fifth longitudinal mode in the polymer-coated resonator. The resonance frequency f_r and half width g_r were from fits of Eq. (24) to the acoustic data and corrected according to Eqs. (25) and (26) as discussed in the text. The speed of sound c_{L5} was determined from the acoustic data, k_0 from a calibration to c_{HS} at one temperature, and Eq. (39). The fractional deviations of $Q_r^{-1}=2g_r/f_r$ from the model, where $\Delta Q^{-1}/Q^{-1} \equiv (Q_r^{-1}-Q_{\mathrm{mod}}^{-1})/Q_{\mathrm{mod}}^{-1}$.

T(°C)	τ	f_r(Hz)	g_r(Hz)	c_{L5}(m s^{-1})	$\Delta Q^{-1}/Q^{-1}$
16.683[a]	3.48×10^{-4}	4400.463	37.632		
16.704[a]	4.20×10^{-4}	4475.998	30.068		
16.732[a]	5.18×10^{-4}	4564.867	23.267		
16.767[a]	6.39×10^{-4}	4657.730	18.140		
16.810[a]	7.88×10^{-4}	4755.087	14.323		
16.864[a]	9.72×10^{-4}	4856.674	11.554		
16.939[a]	1.23×10^{-3}	4974.099	9.367		
17.023[a]	1.52×10^{-3}	5083.198	7.986		
17.125[a]	1.88×10^{-3}	5196.312	7.057		
17.252[a]	2.31×10^{-3}	5313.965	6.379		
17.409[a]	2.85×10^{-3}	5436.229	5.908		
17.602[a]	3.52×10^{-3}	5563.682	5.551		
17.841[a]	4.35×10^{-3}	5696.592	5.294		
18.135[a]	5.36×10^{-3}	5835.753	5.098		
18.498[a]	6.61×10^{-3}	5981.701	4.944		
18.946[a]	8.16×10^{-3}	6135.225	4.818		
19.498[a]	1.01×10^{-2}	6297.234	4.701		
20.179[a]	1.24×10^{-2}	6468.838	4.607		
21.020[a]	1.53×10^{-2}	6651.293	4.511		
22.057[a]	1.89×10^{-2}	6846.034	4.423		
23.337	2.33×10^{-2}	7054.846	4.330	135.642	-3.11×10^{-3}
24.915	2.88×10^{-2}	7279.672	4.236	139.961	-3.95×10^{-3}
26.862	3.55×10^{-2}	7522.841	4.142	144.632	-4.16×10^{-3}

[a]Point omitted from the analysis.

the critical region above T_c and in Ref. [22] the value $C_1=5.9368$ was determined from vapor pressure data below T_c. We used the values of $(\partial P/\partial T)_\rho$ from Ref. [21] and we took the difference between the two values of C_1(0.2%) as an estimate of the uncertainty of $(\partial P/\partial T)_\rho$. The uncertainties of χ_T and c_{HS} are on the order of 0.1%; therefore the uncertainty of our values of C_V is approximately 0.4%.

Kline and Carome [19] determined C_V for xenon in the critical region from their sound speed measurements at 6 kHz. Since they too used the *PVT* data of Habgood and Schneider [21] to determine $(\partial P/\partial T)_\rho$, we estimate their uncertainty in C_V is 2%. Above $\tau=3\times10^{-3}$ Kline and Carome's values of C_V are about 1% higher than ours, whereas below $\tau=3\times10^{-3}$ their values are about 1% lower than ours. In contrast, our values of C_V are much smaller (by 11% at $\tau=10^{-3}$; by 9% at $\tau=10^{-2}$; and by 6% at $\tau=0.035$) than the values of C_V measured by Edwards, Lipa, and Buckingham using a calorimeter [23]. Edwards *et al.* report a systematic uncertainty that ranges from 6% at $\tau=0.001$ to 12% at $\tau=0.035$. To summarize, we believe the present values of C_V are the most accurate available in the range $10^{-3}\leqslant\tau\leqslant10^{-1}$.

We fit the scaled data $C_V^*=T_c\rho_c C_V/P_c$ with the function

$$C_V^* = A^+\tau^{-\alpha}(1+C^+\tau^{0.5})+B^+, \tag{34}$$

using $\alpha=0.110$, to determine the amplitude A^+. Our result $A^+=18.01\pm0.11$ is 8% lower than the value from Edwards *et al.* as reported in Ref. [20]. The correlation length amplitude ξ_0^+ was determined from the principle of two-scale-factor universality [24],

$$\frac{\alpha P_c A^+(\xi_0^+)^3}{k_B T_c} = 0.0188\pm0.0001, \tag{35}$$

where k_B is the Boltzmann constant. The value $\xi_0^+=(0.1866\pm0.0010)$ nm, which we obtained from Eq. (35), agrees with the value (0.184 ± 0.009) nm from Ref. [20] within the combined uncertainties.

The thermal conductivity was deduced by comparing the measurements of the Q of the Helmholtz mode in the steel resonator with the predictions of Eq. (30). This comparison required, as inputs, the effusivity of stainless steel, the diffusivity of stainless steel, and the shear viscosity of xenon measured in microgravity by Berg, Moldover, and Zimmerli [15]. We represented the shear viscosity with a polynomial function of $\log_{10}(\tau)$; the coefficients are listed in Table VII.

The thermal conductivity was expressed in the form

$$\lambda_T = \lambda_{b0}+\lambda_{b1}\tau+\lambda_{b2}\log_{10}(\tau)+\lambda_{b3}[\log_{10}(\tau)]^2+\rho C_P\frac{Rk_BT}{6\pi\eta\xi}, \tag{36}$$

where the parameters λ_{b0}, λ_{b1}, λ_{b2}, and λ_{b3} were adjusted to fit the data and are listed in Table VIII. The last term in Eq. (36) is the critical part of the thermal conductivity, where $\xi=\xi_0^+\tau^{-\upsilon}(\upsilon=0.63)$ is the correlation length and $R=1.05$ [21]. The thermal diffusivity calculated from Eqs. (32) and (36) is within 10% of the values reported by Swinney and Henry [21] over the range of the fit.

An uncertainty in the ratio of the integrals in Eq. (19) propagates into an uncertain scale factor for the thermal conductivity. The ratio of integrals from the numerical modeling was 147.80 m^{-1}; it was adjusted to 149.45 m^{-1} to best fit the data. This adjustment (1.1%) is a systematic uncertainty in the values of the thermal conductivity given by Eq. (36). After λ_T was determined using the stainless steel cell, the Q's of the longitudinal modes of the steel cell could be fit without additional parameters. The same values of λ_T also fit the Q's of the Helmholtz mode of the polymer-coated resonator, provided the effusivity of the polymer was adjusted to the value 370 kg K^{-1} s$^{-5/2}$. As shown in Fig. 5, this value accounts for the Q's of the Helmholtz mode of the polymer-coated resonator to within ±0.2% over the entire range of the data. The same values of λ_T and ε account for the Q's of the longitudinal modes of the polymer-coated resonator.

C. Model of the longitudinal modes

From a lumped-impedance analysis similar to the one in Ref. [2], the complex frequency for the nth longitudinal mode of chamber 1 is given by

TABLE VII. Thermodynamic and transport properties obtained from the literature.

Symbol	Value	Symbol	Value
ρ_c(kg m^{-3})	1116.0±1.7[a]	α	0.110±0.003[b]
P_c(MPa)	5.84[c]	β	0.325±0.002[b]
R	1.05[d]	ν	0.630±0.002[b]
Susceptibility[e]	$\chi_T=(\rho_c^2/P_c)\chi_T^*$,	$\chi_T^*=\Gamma^+\tau^{-\gamma}[1+a_1\tau^{\Delta}+a_2\tau^{2\Delta}+a_3\tau^{3\Delta}]$	
Γ^+	0.0577±0.0001	a_1	1.29±0.03
Δ	0.496	a_2	−1.55±0.2
γ	1.241±0.002	a_3	1.9±0.5
$(\partial P/\partial T)_\rho=(P_c/T_c)(\partial P^*/\partial T^*)_\rho$,	$(\partial P^*/\partial T^*)_\rho$ given by Eq. (33)		
C_1	5.9253[d]	$\rho_c H_2^+$	−1.9201[d]
P_1^+	2.1122[d]		
Shear visocosity[f]	$\eta(\mu\text{Pa s})=h_0+\sum_{n=1}^{5} h_n[\log_{10}(\tau)]^n$		
h_0	62.386	h_3	1.9906
h_1	15.300	h_4	0.29167
h_2	8.0579	h_5	0.01797

[a]See Ref. [26].
[b]See Ref. [27].
[c]See Ref. [28].
[d]See Ref. [21].
[e]See Ref. [20].
[f]This function reproduces the shear viscosity from Ref. [15] to ±0.05 μPa s. The experimental uncertainty was ±0.024 μPa s [15].

$$\frac{F_{Ln}}{f_{0n}} = (1+\Delta_n)\sqrt{\frac{(1+\vartheta)[1-(1-i)q_{vn}\delta_v]}{1+\vartheta+(1-i)(\gamma-1)q'_{Tn}\delta_T}}, \quad (37)$$

where $f_{0n}=k_{0n}c/(2\pi)$, and Δ_n is the solution of

$$\tan\left(\frac{k_{0n}L_c\Delta_n}{2}\right) = -\left[\frac{(1-i)(\gamma-1)q''_{Tn}\delta_T}{1+\vartheta+(1-i)(\gamma-1)q'_{Tn}\delta_T}\right] \times \frac{k_{0n}L_c}{4}(1+\Delta_n). \quad (38)$$

The geometric factor q_{Tn} has been divided into a contribution $q'_{Tn}=q_{Tn}L_c/(L_c+2R_c)$ from the cylindrical sides and a contribution $q''_{Tn}=q_{Tn}-q'_{Tn}$ from the end plates. The speed of sound consistent with measurements with these modes is determined by

$$c_{Ln} = \frac{2\pi(f_r+g_r-g_b)}{k_{0n}[\mathrm{Re}(F_{Ln}/f_{0n})+\mathrm{Im}(F_{Ln}/f_{0n})]}, \quad (39)$$

and the total dissipation is

TABLE VIII. Critical amplitudes and thermal conductivity for xenon from this work. Also effusivities of stainless steel and the polymer coating.

Symbol	Value	Symbol	Value
T_c(°C)	16.583±0.015	ξ_0^+(nm)	0.1866±0.001
A^+	18.015±0.27	R_B	0.0427
B^+	−18.04±0.27	ε_{ss}(kg K^{-1} s$^{-5/2}$)	6389
C^+	0.42±0.1	ε_{pr}(kg K^{-1} s$^{-5/2}$)	368.4
Thermal conductivity λ_T given by Eq. (36)			
λ_{b0}(J K^{-1} m^{-1})	0.01851	λ_{b2}(J K^{-1} m^{-1})	0.005415
λ_{b1}(J K^{-1} m^{-1})	−0.005811	λ_{b3}(J K^{-1} m^{-1})	0.002067

TABLE IX. Dimensions and mode parameters of the bare stainless steel resonator.

r_d(m)	0.00200	r'_d(m)	0.00300
L_d(m)	0.01475	L_i(m)	0.01176
R_{c1}(m)	0.00800	R_{c2}(m)	0.01175
L_{c1}(m)	0.04800	L_{c2}(m)	0.02220
Mode	k_0(m^{-1})	q_v(m^{-1})	q_T(m^{-1})
Helmholtz	12.314	470.07	149.45
1st long.	65.79	164.45	165.03
2nd long.	129.57	136.49	178.92
3rd long.	195.86	130.57	166.91
4th long.	260.98	123.13	171.67
5th long.	326.23	125.00	168.34

$$Q_{Ln}^{-1} = \frac{2\ \mathrm{Im}(F_{Ln})}{\mathrm{Re}(F_{Ln})} + Q_{\zeta n}^{-1}. \tag{40}$$

The results of these measurements are shown in Figs. 4–8. The calculated viscous dissipation has been subtracted from the total measured dissipation and the difference has been plotted as a function of the reduced temperature for all the measured modes. The calculated thermal dissipation also is plotted for comparison. The peaks in the deviation plots for the first longitudinal mode (see Fig. 8) are due to interfering modes in the thermostat or the support structure.

The Helmholtz mode in the uncoated resonator was calibrated with argon as discussed above. The other modes were calibrated at $\tau=0.01$ by a small adjustment of k_0 and the polymer thickness such that the speed of sound equaled c_{HS}. The adjusted values of k_0 differed from Mehl's numerical estimates by less than 1%. The adjusted polymer thickness 82 μm was well within the error of the independent measurement (85 ± 15) μm. Figure 4(b) shows the consistency with which the speed of sound was determined from each mode compared to the reference value c_{HS}. The sound-speed measurements from all the modes in the polymer-coated resonator agree to within 0.01%. Likewise, the sound-speed measurements from all the modes in the bare steel resonator agree to within 0.01%. However, the results from the two resonators disagree by as much as 0.1%. The disagreement would be explained if the xenon in the polymer-coated resonator had a 0.15% lower density and a 5-mK higher critical temperature than the xenon in the bare steel resonator. Although a 0.15% density difference and a 5-mK critical temperature difference are both small, we cannot account for either from the known, quantifiable experimental uncertainties. It is possible that a small quantity of xenon leaked out of the polymer-coated resonator during the short time interval in which we cut the crimped fill tube and soldered the tube closed.

TABLE X. Dimensions and mode parameters for the polymer-coated resonator.

r_d(m)	0.00192	r'_d(m)	0.00308
L_d(m)	0.01490	L_i(m)	0.01184
R_{c1}(m)	0.00792	R_{c2}(m)	0.01167
L_{c1}(m)	0.04780	L_{c2}(m)	0.02204
Mode	k_0(m^{-1})	q_v(m^{-1})	q_T(m^{-1})
Helmholtz	11.952	509.65	149.26
1st long.	65.935	166.14	168.11
2nd long.	129.89	137.90	183.16
3rd long.	196.33	120.04	176.76
4th long.	261.69	113.20	181.80
5th long.	326.99	114.92	178.27

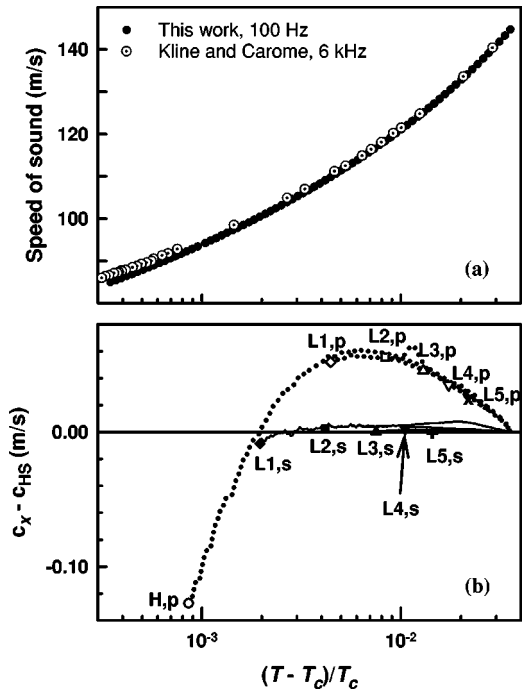

FIG. 4. (a) The speed of sound c_{HS} determined from the Helmholtz mode with bare stainless steel plotted versus the reduced temperature. The speed of sound measured by Kline and Carome [19] at 6 kHz. (b) Deviations of the speed of sound determined from each mode from c_{HS} shown in the upper graph. Note: the six modes for each resonator are mutually consistent at the level of ±0.01% of c_{HS}.

D. Bulk viscosity

In the low-frequency limit, the bulk viscosity is approximately [25]

$$\zeta = \frac{R_B \rho_c c^2 \tau_\xi}{1 + q_B}, \tag{41}$$

where τ_ξ is the relaxation time for critical fluctuations, given by

$$\tau_\xi = \frac{6\pi\xi^3\eta}{k_B T_c}, \tag{42}$$

and q_B is the ratio of the background part of C_V to the singular part of C_V,

$$q_B \equiv \frac{C^*_{V,\text{background}}}{C^*_{V,\text{singular}}} = \frac{C^*_V}{A^+\tau^{-\alpha}} - 1. \tag{43}$$

From our determination of C_V, we found that q_B varied smoothly from −0.6155 at $\tau=0.035$ to −0.4327 at $\tau=0.006$. Theoretical values for the dimensionless constant R_B range from 0.0285 (renormalization group theory) to 0.086 (mode coupling theory) [25]. The value that was consistent with our data was $R_B=0.0427$. The bulk viscosity is predicted [25] to have the strongest temperature dependence ($\sim\tau^{-1.9}$) of any known property and becomes negligible outside the critical region.

The dissipation from bulk viscosity Q_ζ^{-1} was calculated from Eq. (20) with the low-frequency limit of Onuki's theory [25] for bulk viscosity and used in Eqs. (29), (30), (39), and (40). For the Helmholtz mode in the uncoated resonator, the dissipation from bulk viscosity was less than 0.3% of the total dissipation down to about $\tau=6\times10^{-4}$. Therefore the plot in Fig. 5 is almost entirely the thermal dissipation at the surface of the resonator. For the other modes, only data for which the estimated dissipation from bulk viscosity was less than 0.8% of the total dissipation were included in the deviation plots in Figs. 4(b) and 8.

In the future, we plan to use the resonators described here to measure the bulk viscosity very close to T_c. Using all the acoustic modes discussed here, we will measure the bulk viscosity over nearly two decades in frequency; with the low-frequency Helmholtz mode, we will reach $\omega\tau=1$ closer to T_c than any previous measurements. As we have shown here, the polymer coating will reduce by the thermal boundary dissipation up to a factor of 8 and thereby increase the accuracy with which the volume dissipation from bulk viscosity may be measured. The results closer to T_c and the determination of the bulk viscosity will be the subject of a forthcoming paper.

V. CONCLUSIONS

The measured acoustic dissipation in near-critical xenon shows a prominent plateau for the Helmholtz mode (Fig. 5) and, to a lesser extent, for the longitudinal modes (Figs. 6–8). These results are direct evidence of thermal boundary dissipation being limited by the thermophysical properties of the solid wall.

We demonstrated an eight-fold reduction in the thermal boundary dissipation after coating a stainless steel resonator with a low-effusivity polymer (see Fig. 5). Such a reduction in thermal dissipation will be necessary in order to measure the low-frequency dissipation from bulk viscosity close to the critical point in future experiments.

To analyze the data, we formulated a theory for acoustic dissipation in a fluid that is bounded by a rigid wall with the condition that the temperature and heat flux across the boundary be continuous. The theory is valid both near to and far from the critical point; it includes volume and surface dissipation from thermal conduction, shear viscosity, and bulk viscosity.

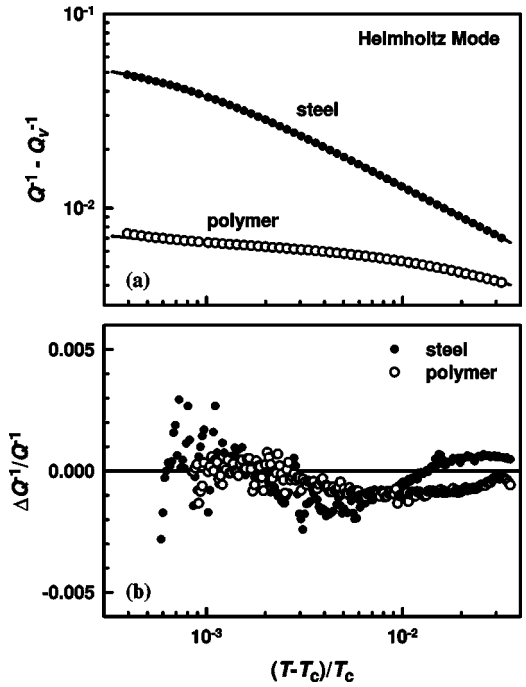

FIG. 5. Comparison of the measured thermal boundary dissipation with theory. (a) The measured thermal boundary dissipation versus reduced temperature for the Helmholtz mode in bare steel (●) and polymer-coated (o) resonators. The bulk viscosity is negligible for the Helmholtz mode in this temperature range. Theory for thermal boundary dissipation (—). (b) The fractional deviations of the measured dissipation from theory versus reduced temperature. We fitted the data for the steel resonator by adjusting the coefficients of λ_T in Table VIII. The data for the polymer-coated resonator were fitted by setting the effusivity of the polymer to the value 370 kg K^{-1} $s^{-5/2}$.

We measured the speed of sound in xenon as a function of reduced temperature in the range $0.0006<\tau<0.03$. Using the measured sound speed and attenuation, the isothermal susceptibility from Ref. [20], and $(\partial P/\partial T)_\rho$ from Ref. [21], we derived C_V, C_P, and the background terms for the thermal conductivity in Eq. (36). These derived properties were used to determine the amplitude $A^+=18.01$ for the singular part of C_V (with $\alpha=0.110$) and the correlation length amplitude $\xi_0^+=0.1866$ nm. Although the data do not extend far into the asymptotic region, the agreement with other values is remarkable.

The onset of bulk viscosity is evident from the excess dissipation (over the thermal and viscous dissipation) indicated by the upturn at low τ of the measured dissipation shown in Figs. 6–8. It is also evident that the dissipation from the bulk viscosity increases as the frequency increases in qualitative agreement with theory. The onset of bulk viscosity is more evident in the polymer-coated resonator because the thermal dissipation is smaller than it is in the bare-steel resonator.

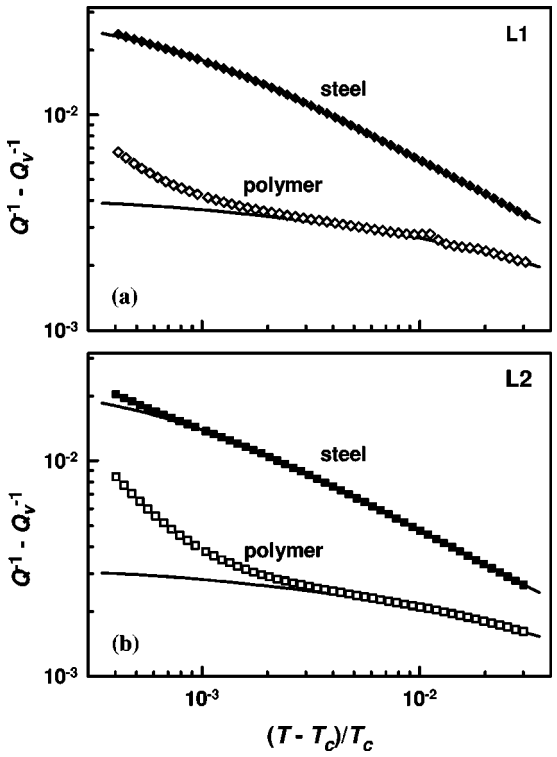

FIG. 6. Dissipation due to bulk viscosity and the thermal boundary layer versus reduced temperature. Two longitudinal modes are shown: (a) L1 for steel (♦) and polymer-coated (◇) resonators and (b) L2 for steel (■) and polymer-coated (□) resonators. Theory for thermal boundary dissipation (—). The small kink in the data for the L1 mode in the polymer-coated resonator near $(T-T_c)/T_c = 10^{-2}$ is caused by an accidental resonance in the thermostat.

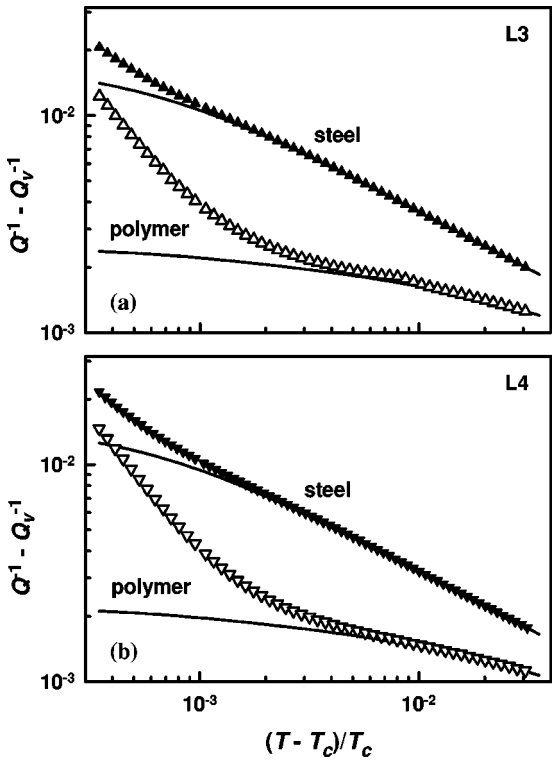

FIG. 7. Dissipation due to bulk viscosity and the thermal boundary layer versus reduced temperature. Two longitudinal modes are shown: (a) L3 for steel (▲) and polymer-coated (△) resonators and (b) L4 for steel (▼) and polymer-coated (▽) resonators. Theory for thermal boundary dissipation (—).

ACKNOWLEDGMENTS

The authors thank Jim Mehl for his expertise, stimulating discussions, and continuing help with numerical calculations of the acoustic modes. We also thank Bobby Berg, Dan Friend, Horst Meyer, Mikhail Anisimov, and Greg Zimmerli for their comments and suggestions regarding this manuscript. This work was funded, in part, by NASA Contract No. C-32088-K.

APPENDIX

In this Appendix, we extend the exact solution [8] for linear acoustic waves in a dissipative fluid to include heat conduction in a rigid wall bounding the fluid. The derived relationships between the fields $\tilde{p}$, $\tilde{T}$, $\tilde{\rho}$, $\tilde{s}$, and $\tilde{\mathbf{u}}$ are valid for single-phase fluids, both near to and far from the critical point, bounded by rigid walls. The walls have finite heat capacity and thermal conductivity.

Equations (3)–(5) support three types of waves: a propagating acoustic wave, a thermal wave, and a shear (vorticity) wave. The thermal and shear waves are evanescent waves and do not propagate. Each of the scalar fields is a sum of two of these waves: an acoustic wave and a thermal wave, i.e.,

$$\tilde{p} = \tilde{p}_{\mathrm{ac}} + \tilde{p}_T, \tag{A1a}$$

$$\tilde{T} = \tilde{T}_{\mathrm{ac}} + \tilde{T}_T, \tag{A1b}$$

$$\tilde{\rho} = \tilde{\rho}_{\mathrm{ac}} + \tilde{\rho}_T, \tag{A1c}$$

$$\tilde{s} = \tilde{s}_{\mathrm{ac}} + \tilde{s}_T. \tag{A1d}$$

The velocity field $\tilde{\mathbf{u}}$ is a sum of all three waves,

$$\tilde{\mathbf{u}} = \tilde{\mathbf{u}}_{\mathrm{ac}} + \tilde{\mathbf{u}}_T + \tilde{\mathbf{u}}_{\mathrm{vor}}. \tag{A1e}$$

The acoustic wave components of the fields are coupled together through Eqs. (3)–(5) and a number of thermodynamic relationships. The thermal wave components are similarly coupled together. The shear wave decouples from the equations for the other waves. The amplitudes of the three types of waves are related to each other only through the boundary conditions Eqs. (7a)–(7d).

We eliminate all the fields but $\tilde{T}$ from Eqs. (3)–(5) to obtain the fourth-order differential equation,

$$\left(\nabla^2 + \frac{\omega^2 q_+^2}{c^2}\right)\left(\nabla^2 + \frac{\omega^2 q_-^2}{c^2}\right)\tilde{T} = 0, \tag{A2}$$

where the full temperature oscillation is written as $\tilde{T} = \tilde{T}_+ + \tilde{T}_-$ such that $\nabla^2 \tilde{T}_\pm = -(\omega q_\pm / c)^2 \tilde{T}_\pm$. The dimensionless wave numbers q_+ and q_- are given by the expressions

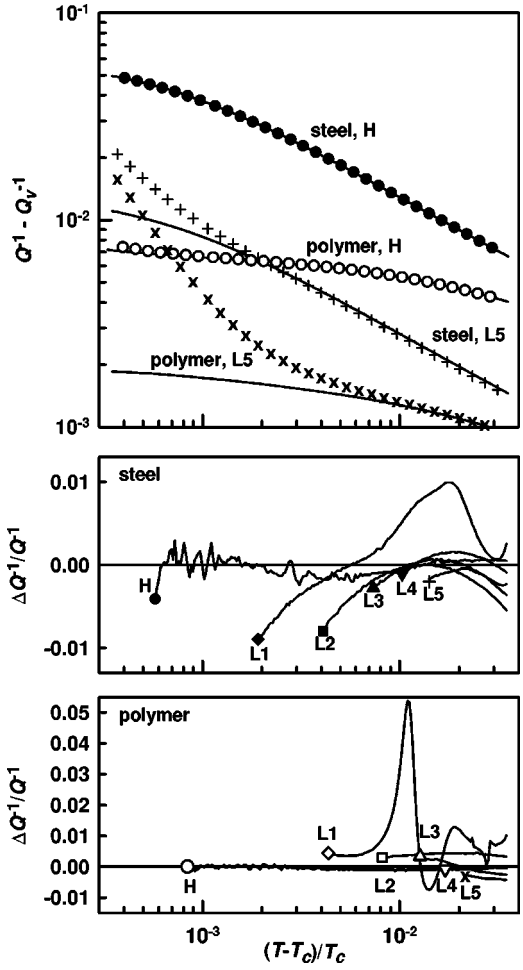

FIG. 8. Dissipation due to bulk viscosity and the thermal boundary layer versus reduced temperature. (a) The lowest and highest frequency modes are shown: the Helmholtz modes (H) for steel (●) and polymer-coated (○) resonators and the fifth longitudinal modes (L5) for steel (+) and polymer-coated (×) resonators. Theory for thermal boundary dissipation (—). (b) The fractional deviations of the measured dissipation from theory versus reduced temperature for all the modes in the steel resonator. (c) Same as (b) but for the polymer-coated resonator. Only data for which the dissipation from bulk viscosity was less than 0.8% of the total dissipation is shown. The peaks in the data for the L1 mode are due to accidental resonances of the thermostat.

$$q_{\pm}^2 = \frac{1 + i\Delta_v + i\gamma\Delta_T \pm \Xi}{2i\Delta_T(1 + i\gamma\Delta_v)}, \tag{A3}$$

where

$$\Delta_v = \frac{\omega}{c^2}\left(\frac{\zeta}{\rho} + \frac{4}{3}D_v\right), \tag{A4}$$

$$\Delta_T = \frac{\omega}{c^2}D_T, \tag{A5}$$

and

$$\Xi^2 = (1 + i\Delta_v - i\gamma\Delta_T)^2 + 4i\Delta_T(\gamma - 1). \tag{A6}$$

(The reader is cautioned not to confuse $q_{\pm}$ with the integral ratios q_v and q_T that are discussed in the main text.) The two solutions $\tilde{T}_{\pm}$ correspond to (i) the propagating acoustic wave $\tilde{T}_{\rm ac}=\tilde{T}_-$ characterized by the wave number $k_{\rm ac}=\omega q_-/c$ and (ii) the thermal wave $\tilde{T}_T=\tilde{T}_+$ characterized by the wave number $k_T=\omega q_+/c$. The other fields $\tilde{p}$, $\tilde{\rho}$, $\tilde{s}$, and $\tilde{\mathbf{u}}_l$ also satisfy Eqs. (A2)–(A6). These fields will be a superposition of acoustic and thermal wave components as well. The relationships among the fields, which are consistent with Eqs. (3)–(5) and (A2)–(A6), are

$$\tilde{p}_{\pm} = \frac{\gamma\overline{\alpha}}{\gamma - 1}\frac{P_c}{T_c}(1 - i\Delta_T q_{\pm}^2)\tilde{T}_{\pm}, \tag{A7}$$

$$\frac{\tilde{\rho}_{\pm}}{\rho} = \frac{q_{\pm}^2}{1 - i\Delta_v q_{\pm}^2}\frac{\tilde{p}_{\pm}}{\rho c^2}, \tag{A8}$$

$$\tilde{s}_{\pm} = \frac{iC_P}{T}\Delta_T q_{\pm}^2 \tilde{T}_{\pm}, \tag{A9}$$

and

$$\tilde{\mathbf{u}}_{l\pm} = -\frac{1}{1 - i\Delta_v q_{\pm}^2}\frac{1}{i\omega\rho}\nabla\tilde{p}_{\pm}. \tag{A10}$$

The quantity

$$\overline{\alpha} \equiv \frac{T_c}{P_c}\left(\frac{\partial P}{\partial T}\right)_{\rho} \tag{A11}$$

is a dimensionless parameter that remains finite at the liquid-vapor critical point ($\overline{\alpha}\approx 6$ for most substances at the critical point). Here, the subscripts + and − refer to the thermal and acoustic wave components, respectively.

As an aside, we note that Δ_v and $(\gamma-1)\Delta_T$ are very small in the dilute-gas limit. To lowest order the wave numbers are

$$k_T \approx (1 - i)\left(\frac{\omega}{2D_T}\right)^{1/2}\left[1 + \frac{i}{2}(\gamma - 1)(\Delta_T - \Delta_v)\right] \tag{A12}$$

and

$$k_{\rm ac} \approx \frac{\omega}{c}\left[1 - \frac{i}{2}\Delta_v - \frac{i}{2}(\gamma - 1)\Delta_T\right]. \tag{A13}$$

These approximations are consistent with the lowest order approximations published elsewhere [8]. The parameter $k_{\rm ac}$ is mostly real with a small imaginary part, consistent with an attenuated propagating wave. In contrast, the parameter k_T has a large imaginary part. Therefore the thermal wave is a heavily damped evanescent wave whose amplitude is significant only near the fluid's boundary.

The shear wave $\tilde{\mathbf{u}}_{\rm vor}$ completely decouples from the other fields. In addition to being divergence free, $\tilde{\mathbf{u}}_{\rm vor}$ satisfies $\nabla^2\tilde{\mathbf{u}}_{\rm vor}=-k_v^2\tilde{\mathbf{u}}_{\rm vor}$ with $k_v=(1-i)/\delta_v$. Like the thermal wave, the shear wave is heavily damped and exists only near the boundary. Since the acoustic wave alone cannot always sat-

isfy all the boundary conditions simultaneously, just enough of the thermal and shear waves are present to satisfy these conditions.

To proceed, we will zoom in on a small portion of the fluid/solid interface. The distance from the wall will be designated the coordinate x. The coordinates y and z give the distance parallel to the wall. The spatial dependence of the wave fields separates into two functions that describe wave motion perpendicular and parallel to the wall. For the acoustic pressure, we write

$$\tilde{p}_{\rm ac} = \tilde{p}_{\rm ac1}\Phi(x)\Psi(y,z)e^{i\omega t}. \tag{A14}$$

The functions $\Phi(x)$ and $\Psi(y,z)$ satisfy the separate wave equations

$$\frac{d^2\Phi}{dx^2} = -k_{{\rm ac}\perp}^2\Phi \text{ and } \boldsymbol{\nabla}_\parallel^2\Psi = -k_{{\rm ac}\parallel}^2\Psi, \tag{A15}$$

where $k_{{\rm ac}\perp}^2 + k_{{\rm ac}\parallel}^2 = k_{\rm ac}^2$ and $\boldsymbol{\nabla}_\parallel^2 = (\partial^2/\partial y^2) + (\partial^2/\partial z^2)$. If θ is the incident angle measured from the surface normal, then $k_{{\rm ac}\parallel} = k_{\rm ac}\sin\theta$.

Likewise, the thermal wave has the form

$$\tilde{T}_T(\mathbf{r},t) = \tilde{T}_{T1}\Theta(x)\Psi(y,z)e^{i\omega t} \tag{A16}$$

such that

$$\frac{d^2\Theta}{dx^2} = -k_{T\perp}^2\Theta = -k_T^2(\cos^2\varphi_T)\Theta \tag{A17}$$

and $k_{T\perp}^2 + k_{{\rm ac}\parallel}^2 = k_T^2 = (\omega q_+/c)^2$ in accordance with Eq. (A2). Here, the angle φ_T is given by

$$\sin\varphi_T = \tfrac{1}{2}(1+i)\delta_T k_{\rm ac}\sin\theta, \tag{A18}$$

and the thermal penetration length in the fluid δ_T, defined by $\delta_T^2 \equiv -2i/k_T^2$, is

$$\delta_T = \left(\frac{2D_T}{\omega}\right)^{1/2}\left[\frac{2(1+i\gamma\Delta_v)}{1+i\Delta_v+i\gamma\Delta_T+\Xi}\right]^{1/2}. \tag{A19}$$

On the scale of δ_v and δ_T, the wall appears as an infinite flat plane. If the solid wall occupies the half space $x<0$, the plane-wave form for the thermal wave in the fluid is

$$\Theta(x) = \exp[-(1+i)x\cos\varphi_T/\delta_T]. \tag{A20}$$

Far from the critical point, δ_T is indistinguishable from $(2D_T/\omega)^{1/2}$. Indeed, for the data presented here δ_T differs from $(2D_T/\omega)^{1/2}$ by less than 0.6%. As the critical point is approached, the theory predicts that $|\delta_T|$ at first decreases approximately as $\tau^{0.4}$ (effective exponent), while Im (δ_T) grows. The minimum value of $|\delta_T|$ is expected to occur when $\gamma\Delta_v \approx 0.5$ corresponding to $\tau = 4\times10^{-4}$ for the Helmholtz mode and $\tau = 1\times10^{-3}$ for the L5 mode. As discussed in the Introduction, we identify the location of this minimum as the transition between the classical and viscous regimes, as defined by Carlés and Zappoli [3]. This coincides with the appearance of a pressure gradient within the boundary layer. The location of the minimum value for all the modes was outside the range of data analyzed for this work. Closer to the critical point, Eq. (A19) predicts that

$$\delta_T \approx (1+i)\left(\frac{2D_T}{\omega}\right)^{1/2}\left[\frac{\gamma\Delta_v}{2(1+i\Delta_v)}\right]^{1/2} \tag{A21}$$

with a magnitude approaching $|\delta_T| \approx 100(2D_T/\omega)^{1/2}$ at $\tau \approx 1\times10^{-6}$. Further details of this phenomenon are beyond the scope of this paper. A full discussion will be included in a forthcoming publication on the analysis of data very close to T_c.

Similarly in the solid, we seek the solution to the diffusion equation

$$\boldsymbol{\nabla}^2\tilde{T}_s = -k_{Ts}^2\tilde{T}_s = \frac{2i}{\delta_{Ts}^2}\tilde{T}_s \tag{A22}$$

that remains finite as $x\to-\infty$ and satisfies the boundary conditions (7c) and (7d). The desired solution has the form

$$\tilde{T}_s(\mathbf{r},t) = \tilde{T}_{s1}\Psi(y,z)\exp[(1+i)x\cos\varphi_{Ts}/\delta_{Ts}]e^{i\omega t}, \tag{A23}$$

where

$$\sin\varphi_{Ts} = \tfrac{1}{2}(1+i)\delta_{Ts}k_{\rm ac}\sin\theta \tag{A24}$$

so that $k_{Ts\perp} = k_{Ts}\cos\varphi_{Ts} = \sqrt{k_{Ts}^2 - k_{ac\parallel}^2}$.

The divergence-free (transverse) velocity field $\tilde{\mathbf{u}}_{\mathbf{vor}}$ that satisfies

$$\boldsymbol{\nabla}^2\tilde{\mathbf{u}}_{\mathbf{vor}} = -k_v^2\tilde{\mathbf{u}}_{\rm vor} = \frac{2i}{\delta_v^2}\tilde{\mathbf{u}}_{\rm vor} \tag{A25}$$

with $\boldsymbol{\nabla}\cdot\tilde{\mathbf{u}}_{\mathbf{vor}} = 0$ has the form

$$\tilde{\mathbf{u}}_{\mathbf{vor}}(\mathbf{r},t) = \tilde{\mathbf{u}}_{v1}(y,z,t)\exp[-(1+i)x(\cos\varphi_v)/\delta_v], \tag{A26}$$

where $\sin\varphi_v = \tfrac{1}{2}(1+i)\delta_v k_{ac}\sin\theta$ and $k_v\cos\varphi_v = \sqrt{k_v^2 - k_{ac\parallel}^2}$.

The boundary conditions [Eqs. (7a)–(7d)] on the total velocity and temperature fields can be recast into a boundary condition on the acoustic wave,

$$\begin{aligned}\hat{\mathbf{n}}\cdot\tilde{\mathbf{u}}_{\rm ac}(0) = {}& \frac{(1-i)\delta_v}{2\cos\varphi_v}\boldsymbol{\nabla}_\parallel\cdot\tilde{\mathbf{u}}_{\rm ac}(0) + \frac{(1+i)}{2\omega\rho}\frac{k_{\rm ac}^2\delta_T\cos\varphi_T}{1-i\Delta_v q_-^2} \\ & \times\frac{1-i\gamma\Delta_T q_+^2}{1-i\gamma\Delta_T q_-^2}\frac{1+\tan\varphi_T\tan\varphi_v}{\cos\varphi_{Ts}+\vartheta\cos\varphi_T} \\ & \times\left[\cos\varphi_{Ts}\tilde{p}_{\rm ac}(0) - \tfrac{1}{2}(1-i)\vartheta\delta_T\hat{\mathbf{n}}\cdot\boldsymbol{\nabla}_\perp\tilde{p}_{\rm ac}(0)\right],\end{aligned} \tag{A27}$$

where

$$\vartheta \equiv \frac{\varepsilon}{\varepsilon_s}\left[\frac{1+i\Delta_V+i\gamma\Delta_T+\Xi}{2(1+i\gamma\Delta_V)}\right]^{1/2}. \tag{A28}$$

In terms of the acoustic pressure alone, the boundary condition on the acoustic wave is

$$\hat{\mathbf{n}}\cdot\boldsymbol{\nabla}_{\perp}\tilde{p}_{\mathrm{ac}}(0)=\frac{ik_{\mathrm{ac}}\tilde{p}_{\mathrm{ac}}(0)}{\mathcal{L}}\Bigg[(\cos\varphi_{Ts}+\vartheta\cos\varphi_T)\sin\theta\tan\varphi_v-\frac{(1+i)}{2}\frac{1-i\gamma\Delta_T q_+^2}{1-i\gamma\Delta_T q_-^2}(1+\tan\varphi_T\tan\varphi_v)\times k_{\mathrm{ac}}\delta_T\cos\varphi_T\cos\varphi_{Ts}\Bigg], \tag{A29}$$

where

$$\mathcal{L}\equiv\cos\varphi_{Ts}+\vartheta\cos\varphi_T\times\left[1-\frac{i}{2}\frac{1-i\gamma\Delta_T q_+^2}{1-i\gamma\Delta_T q_-^2}(1+\tan\varphi_T\tan\varphi_v)k_{\mathrm{ac}}^2\delta_T^2\right]. \tag{A30}$$

Equations (A27)–(A30), with Eq. (A10), lead to an expression for the effective acoustic admittance of the boundary layer per unit area,

$$\beta_{\mathrm{ac}}\equiv-\frac{\rho c\hat{\mathbf{n}}\cdot\tilde{\mathbf{u}}_{\mathrm{ac}}(0)}{\tilde{p}_{\mathrm{ac}}(0)}=\frac{(1+i)k_{\mathrm{ac}}^2}{1-i\Delta_v q_-^2}\frac{c}{2\omega}\Bigg[\frac{\delta_v\sin^2\theta}{\cos\varphi_v}-\frac{1-i\gamma\Delta_T q_+^2}{1-i\gamma\Delta_T q_-^2}\times(1+\tan\varphi_T\tan\varphi_v)\mathcal{K}\delta_T\cos\varphi_T\Bigg], \tag{A31}$$

where

$$\mathcal{K}\equiv\frac{1}{\mathcal{L}}(\cos\varphi_{Ts}-\vartheta\sin\varphi_T\tan\varphi_v). \tag{A32}$$

In the dilute gas limit, Eq. (A31) reduces to

$$\beta_{\mathrm{ac}}\approx(1+i)\frac{\omega}{2c}[\delta_v\sin^2\theta+(\gamma-1)\delta_T] \tag{A33}$$

in agreement with Morse and Ingard [8].

In terms of the acoustic pressure $\tilde{p}_{\mathrm{ac}}$, the resultant fields are

$$\tilde{T}=\frac{\gamma-1}{\gamma\bar{\alpha}}\frac{T_c}{P_c}\frac{1}{1-i\Delta_T q_-^2}\{\tilde{p}_{\mathrm{ac}}-\mathcal{K}\tilde{p}_{\mathrm{ac}}(0)\times\exp[-(1+i)x\cos\varphi_T/\delta_T]\}, \tag{A34}$$

$$\tilde{T}_s=\frac{\gamma-1}{\gamma\bar{\alpha}}\frac{T_c}{P_c}\frac{\mathcal{J}}{1-i\Delta_T q_-^2}\left(1-\frac{i}{2}\frac{1-i\gamma\Delta_T q_+^2}{1-i\gamma\Delta_T q_-^2}k_{\mathrm{ac}}^2\delta_T^2\right)\tilde{p}_{\mathrm{ac}}(0)\times\exp[(1+i)x\cos\varphi_{Ts}/\delta_{Ts}], \tag{A35}$$

$$\tilde{p}=\tilde{p}_{\mathrm{ac}}-\frac{1-i\Delta_T q_+^2}{1-i\Delta_T q_-^2}\mathcal{K}\tilde{p}_{\mathrm{ac}}(0)\exp[-(1+i)x\cos\varphi_T/\delta_T], \tag{A36}$$

$$\tilde{\rho}=\frac{1}{1-i\Delta_v q_-^2}\frac{k_{\mathrm{ac}}^2}{\omega^2}\left\{\tilde{p}_{\mathrm{ac}}-\frac{1-i\gamma\Delta_T q_+^2}{1-i\gamma\Delta_T q_-^2}\mathcal{K}\tilde{p}_{\mathrm{ac}}(0)\times\exp[-(1+i)x\cos\varphi_T/\delta_T]\right\}, \tag{A37}$$

$$\tilde{s}=\frac{i\lambda_T T_c}{\rho\omega P_c T}\frac{\gamma-1}{\gamma\bar{\alpha}}\frac{1}{1-i\Delta_T q_-^2}\{k_{\mathrm{ac}}^2\tilde{p}_{\mathrm{ac}}-k_T^2\mathcal{K}\tilde{p}_{\mathrm{ac}}(0)\times\exp[-(1+i)x\cos\varphi_T/\delta_T]\}, \tag{A38}$$

$$\tilde{\mathbf{u}}_{\mathrm{ac}}=-\frac{1}{1-i\Delta_v q_-^2}\frac{\boldsymbol{\nabla}\tilde{p}_{\mathrm{ac}}}{i\omega\rho}, \tag{A39}$$

$$\tilde{\mathbf{u}}_T=\frac{k_{\mathrm{ac}}^2\delta_T}{2\rho\omega}\frac{1-i\gamma\Delta_T q_+^2}{1-i\gamma\Delta_T q_-^2}\frac{\mathcal{K}}{1-i\Delta_v q_-^2}[\delta_T\boldsymbol{\nabla}_{\parallel}\tilde{p}_{\mathrm{ac}}(0)-\hat{\mathbf{n}}(1+i)\tilde{p}_{\mathrm{ac}}(0)\cos\varphi_T]\times\exp[-(1+i)x\cos\varphi_T/\delta_T], \tag{A40}$$

and

$$\tilde{\mathbf{u}}_{\mathrm{vor}}=\frac{1}{i\omega\rho}\frac{\mathcal{J}+\mathcal{K}}{1-i\Delta_v q_-^2}\left(1-\frac{i}{2}\frac{1-i\gamma\Delta_T q_+^2}{1-i\gamma\Delta_T q_-^2}k_{\mathrm{ac}}^2\delta_T^2\right)\times[\boldsymbol{\nabla}_{\parallel}\tilde{p}_{\mathrm{ac}}(0)+\hat{\mathbf{n}}ik_{\mathrm{ac}}\tilde{p}_{\mathrm{ac}}(0)\sin\theta\tan\varphi_v]\times\exp[-(1+i)x\cos\varphi_v/\delta_v], \tag{A41}$$

where

$$\mathcal{J}\equiv\frac{\vartheta}{\mathcal{L}}(1+\tan\varphi_T\tan\varphi_v)\cos\varphi_T. \tag{A42}$$

[1] For work on ^{3}He, ^{4}He, and mixtures, see D. B. Roe, B. A. Wallace, and H. Meyer, J. Low Temp. Phys. **16**, 51 (1974); D. B. Roe and H. Meyer, *ibid.* **30**, 91 (1978); T. Doiron, D. Gestrich, and H. Meyer, Phys. Rev. B **22**, 3202 (1980); for work on xenon, see C. W. Garland and R. D. William, Phys. Rev. A **10**, 1328 (1974); P. E. Mueller, D. Eden, C. W. Garland, and R. C. Williamson, *ibid.* **6**, 2272 (1973); J. Thoen and C. W. Garland, *ibid.* **10**, 1311 (1974).

[2] K. A. Gillis, J. B. Mehl, and M. R. Moldover, J. Acoust. Soc. Am. **114**, 166 (2003).

[3] P. Carlés and B. Zappoli, Phys. Fluids **7**, 2905 (1995); P. Carlés, *ibid.* **10**, 2164 (1998).

[4] K. A. Gillis, J. B. Mehl, and M. R. Moldover, Rev. Sci. Instrum. **67**, 1850 (1996).

[5] J. Wilhelm, K. A. Gillis, J. B. Mehl, and M. R. Moldover, Int. J. Thermophys. **21**, 983 (2000).

[6] J. J. Hurly, K. A. Gillis, J. B. Mehl, and M. R. Moldover, Int. J. Thermophys. **24**, 1441 (2003).

[7] Allan D. Pierce, *Acoustics: An Introduction to Its Physical Principles and Applications* (McGraw-Hill, New York, 1981), Chap. 10.
[8] P. M. Morse and K. U. Ingard, *Theoretical Acoustics* (McGraw-Hill, New York, 1968).
[9] G. Kirchhoff, Annalen der Physik und Chemie **134**, 177 (1868), translated in *Physical Acoustics*, edited by R. B. Lindsay (Dowden, Hutchinson, and Ross, Stroudsburg, PA, 1974).
[10] M. R. Moldover, J. B. Mehl, and M. Greenspan, J. Acoust. Soc. Am. **79**, 253 (1986); M. R. Moldover, J. P. M. Trusler, T. J. Edwards, J. B. Mehl, and R. S. Davis, J. Res. Natl. Bur. Stand. **93**, 85 (1988).
[11] M. Bruneau, Ph. Herzog, J. Kergomard, and J. D. Polack, Wave Motion **11**, 441 (1989).
[12] J. P. M. Trusler, *Physical Acoustics and Metrology of Fluids* (Adam Hilger, Bristol, 1991).
[13] J. B. Mehl, NIST Technical Report, 2002.
[14] In order to describe materials and experimental procedures adequately, it is occasionally necessary to identify commercial products by the manufacturer's name or label. In no instance does such identification imply endorsement by the National Institute of Standards and Technology, nor does it imply that the particular product or equipment is necessarily the best available for the purpose.
[15] R. F. Berg, M. R. Moldover, and G. A. Zimmerli, Phys. Rev. E **60**, 4079 (1999); R. F. Berg, M. R. Moldover, and G. A. Zimmerli, Phys. Rev. Lett. **82**, 920 (1999).
[16] R. F. Berg, G. A. Zimmerli, and M. R. Moldover, Int. J. Thermophys. **19**, 481 (1998).
[17] E. W. Lemmon, M. O. McLinden, and M. L. Huber, "NIST standard reference database 23: Reference fluid thermodynamic and transport properties, version 7.0," National Institute of Standards and Technology, Standard Reference Data Program, Gaithersburg, MD, 2002.
[18] M. R. Moldover, J. V. Sengers, R. W. Gammon, and R. J. Hocken, Rev. Mod. Phys. **51**, 79 (1979).
[19] J. L. Kline and E. F. Carome, J. Chem. Phys. **58**, 4962 (1973).
[20] H. Güttinger and D. S. Cannell, Phys. Rev. A **24**, 3188 (1981).
[21] H. L. Swinney and D. L. Henry, Phys. Rev. A **8**, 2566 (1973). The representation of $(\partial P/\partial T)_\rho$ given by Swinney and Henry was a fit to measurements by H. W. Habgood and W. G. Schneider, Can. J. Chem. **32**, 98 (1954).
[22] V. G. Baidakov, A. M. Rubshteyn, and V. P. Pomortsev, Fluid Mech. Res. **21**, 89 (1992).
[23] C. Edwards, J. A. Lipa, and M. J. Buckingham, Phys. Rev. Lett. **20**, 496 (1968).
[24] M. E. Fisher and S. Y. Zinn, J. Phys. A **31**, L629 (1998).
[25] Akira Onuki, Phys. Rev. E **55**, 403 (1997); Akira Onuki, *Phase Transition Dynamics* (Cambridge University Press, Cambridge, England, 2002), Chap. 6.
[26] U. Närger and D. A. Balzarini, Phys. Rev. B **42**, 6651 (1990).
[27] V. A. Agayan, M. A. Anisimov, and J. V. Senegers, Phys. Rev. E **64**, 026125 (2001).
[28] J. V. Senegers and J. M. H. Senegers, Annu. Rev. Phys. Chem. **37**, 189 (1996).